Coupled thermo-electro-mechanical topology optimization for cooling applications under electrical constraints

Reales Gutiérrez, G.; Aragón, A. M.; Goosen, H. F.L.; Bornheim, A.; van Keulen, A.

DOI
10.1007/s00158-025-04087-8

Publication date
2025

Document Version
Final published version

Published in
Structural and Multidisciplinary Optimization

Citation (APA)
Reales Gutiérrez, G., Aragón, A. M., Goosen, H. F. L., Bornheim, A., & van Keulen, A. (2025). Coupled thermo-electro-mechanical topology optimization for cooling applications under electrical constraints. *Structural and Multidisciplinary Optimization*, *68*(7), Article 141. https://doi.org/10.1007/s00158-025-04087-8

Structural and Multidisciplinary Optimization (2025) 68:141
https://doi.org/10.1007/s00158-025-04087-8

RESEARCH PAPER

Coupled thermo-electro-mechanical topology optimization for cooling applications under electrical constraints

G. Reales Gutiérrez[1] · A. M. Aragón[1] · H. F. L. Goosen[1] · A. Bornheim[2] · F. van Keulen[1]

Received: 31 January 2025 / Revised: 20 May 2025 / Accepted: 10 July 2025

Abstract

This paper addresses the topology optimization of thermocouples for cooling applications, considering stress constraints to enhance reliability under service loads. We provide a first approach to derive sensitivities using SIMP (solid isotropic material with penalization) for thermo-electro-mechanical systems with temperature-dependent material properties. The proposed formulation decouples the thermoelectrical system from the mechanical degrees of freedom reducing computational memory usage from a fully coupled approach. The study focuses on the formulation of thermocouples for cooling applications using the Peltier effect, which considers electrical power limits, electrical working points, and material stress thresholds. Furthermore, while the thermoelectrical problem does not show the need for filtering techniques, including the mechanical degrees of freedom, we show that we recover undesirable porous optimized designs. We provide 2D thermocouple example optimizations with geometries and boundary conditions based on a practical case for the implementation of thermoelectric coolers in the Minimum Ionizing Particle Timing Detector (MTD) at CERN. The optimizations are performed with increased complexity, including the unfiltered thermoelectrical and thermo-electro-mechanical problems and a Helmholtz-filtered examples. The optimizations are compared with constant and nonlinear material properties with temperature and with respect to the consideration of air-conductance losses within the devices. Although more efficient topologies can be achieved without the need for volume constraints, we include an example with a constraint of 60% volume to understand its effect on the design and provide a methodology to reduce semiconductor-associated costs at lower efficiency costs. Finally, we explore the same formulation in 3D. The results provide guidelines for manufacturing compliant thermocouples, increasing their reliability without decreasing efficiency.

Keywords Topology optimization · Thermoelectric-cooler (TEC) · Power constraint · Temperature minimization · SIMP · Non-convexity · Stress constraint

1 Introduction

Thermoelectric coolers utilize the Peltier effect to induce a heat flux by connecting dissimilar semiconductor materials. Compared to traditional vapour compression refrigeration, thermoelectric cooling offers static operation, miniaturization, subambient temperature capability, high reliability, absence of gaseous emissions, and noiseless operation. These benefits have led to the application of Thermoelectric Coolers (TECs) in diverse fields such as cryogenics (Goswami and Kanetkar 2020), on-chip thermal management (Chen et al. 2022b), laser and fibre optics with precise temperature regulation requirements (Gupta et al. 2024; Zhang et al. 2015), medical devices (Zaferani et al. 2021), and localized cooling in space vehicles (Singh et al. 2023). Despite ongoing research on its large-scale implementation, such as building refrigeration (Duan et al. 2021), cost-effectiveness remains a challenge due to its lower efficiencies compared to vapour compression systems. These lower efficiencies are due to the need to balance the properties of

---

Responsible Editor: Emilio Carlos Nelli Silva.

✉ G. Reales Gutiérrez
g.realesguti@gmail.com; grealesgutierr@tudelft.nl; guillermo.reales@cern.ch

[1] Faculty of Mechanical Engineering, Delft University of Technology, Mekelweg 2, 2628 CD, Delft, The Netherlands

[2] California Institute of Technology-High Energy Physics, 1200 E California Blvd, Pasadena, CA 91125, USA

the thermoelectric material within the semiconductor components (Al-Fartoos et al. 2023).

The material composition of a TEC determines its intrinsic properties. However, the arrangement of materials in each semiconductor leg can also modify the device's overall characteristics. The impact of the semiconductor leg shape was investigated in Fabián-Mijangos et al. (2017), who provided a manufacturing method and demonstrated a higher efficiency for asymmetric pyramidal or trapezoidal thermocouple shapes compared to regular cubic shapes. In Sun et al. (2024), these shapes are combined with segmented legs containing more than a single semiconductor material to train a neural network to provide the optimal combination of geometric parameters and output power. Additionally, topology optimization (TO) through the SIMP (solid isotropic material with penalization) method with volume constraints can be employed to improve the efficiency of heat recovery thermoelectric devices. Takezawa and Kitamura (2012) introduce this methodology for thermoelectric generators with all material penalization coefficients equal to unity and a 1D model to validate the sensitivities. In Xu et al. (2019), the previous method is extended to segmented semiconductor legs using multimaterial TO. There is also literature on the system integration of thermoelectrical devices with Soprani et al. (2016), optimizing the thermal coupling material from the TECs to its thermal contacts with simplifications of the thermoelectrical module as a single material block for a downhole oil well intervention tool. Finally, Lundgaard and Sigmund (2018) examine the TO formulation for different thermoelectrical objectives and problem formulations, including power output, conversion efficiency, temperature, heat flux, and coefficient of performance using two different materials in direct contact. Together, these studies highlight the importance of material arrangement and leg optimization in shaping TEC performance.

TO algorithms can reduce semiconductor materials' volume and material costs—up to a third of the system cost (Leblanc et al. 2014)—maintaining efficiency. However, the topology shapes that arise can compromise their mechanical reliability. Mechanical ageing, which occurs from the dissimilar materials in the thermocouple composition, introduces efficiency losses. A single thermocouple involves a solder and an electrode with thermoelastic properties different from the semiconductor's, leading to mechanical loading. Additionally, these devices experience temperature variations through their thickness, influencing the properties of the semiconductor material and the fatigue conditions. This ageing process, which increases electrical resistivity and decreases Seebeck coefficients of the affected thermocouples, decreases efficiency over time. Due to the importance of this efficiency loss, multiple approaches have been proposed to predict it. For instance, Merienne et al. (2019) and Williams et al. (2022) highlight the effect of thermal cycling on commercial thermoelectric generators, revealing the increased resistance due to material cracking over time. Wang et al. (2019) use digital image correlation to experimentally identify the cracking spot at the copper–Bi_2Te_3 interface to provide a diagnostic method. Gong et al. (2019) present a model to estimate thermal loads and proposes improvements over previous models considering copper and ceramic layers. The electrical operation also impacts the ageing process, as demonstrated by Fan et al. (2022), who showed that pulse operation could reduce thermally induced stresses. The effect of the shape of the thermoelectric semiconductor is highlighted in the literature through FEM (finite element method) models. Erturun et al. (2015) look into the effect of the shape of the pellets of the thermo-electro-mechanical performance of thermoelectric generators in ANSYS, and Zhang et al. (2023) use COMSOL to perform similar measures within a thermoelectric cooler and a parametric analysis of the dimensions of the design. Finally, Suhir and Shakouri (2013) develop an analytical model to estimate the shear stress along the bonded layers of a TEC and compare it to an ANSYS model. The results from these works emphasize the higher induced thermal stresses at the edges of the legs and their contact with the solder layer. Different leg designs, including truncated cones or trapezoidal shapes with variable cross-sections, show promise in reducing stress at material interfaces (Liu et al. 2023; Al-Merbati et al. 2013; Lu et al. 2020).

TO can alleviate local stresses, with formulations dating back to Yang and Chen (1996). Verbart (2015) and Yvonnet and Da (2024) summarize recent advances in fracture TO, which presents commonly used stress aggregations to mitigate fatigue and crack initiation in materials. Verbart et al. (2017) outline various options for structural stress aggregation, highlighting their distinct impacts on optimal outcomes. Lastly, Meng et al. (2021) explore the thermoelastic stress-based TO. These techniques are readily applicable to thermoelectric devices, and their thermoelastic behaviour is incorporated to minimize induced thermal stresses and enhance operational reliability. In Mativo et al. (2020), a simplified thermomechanical model using SIMP is further used to reduce shear loading-induced stresses. Another example of designs of thermo-electro-mechanical compliant mechanisms through the level-set method can be found in Furuta et al. (2017) with linear material properties with temperature. In essence, TO methods offer a versatile approach to reducing stress and optimizing thermoelectric device performance and reliability.

There are limited examples of multiphysics thermo-electro-mechanical optimizations considering the Peltier effect in the literature. Some of the relevant work in the field include Furuta et al. (2017), which provides a level-set optimization formulation for thermoelectric mechanical actuators based on the Peltier effect or Xing et al. (2024), which uses a Kriging optimization and COMSOL to optimize a flexible thermoelectric generator without the use of sensitivities. Pérez-Aparicio et al. (2024) perform shape optimization using simulated annealing for transient pulse shapes and associated temperature profiles with limits to the induced stresses using linear elasticity. Chen et al. (2022a) use ANSYS and multi-objective genetic optimization algorithms to reduce stresses in a full thermoelectric module through the parameterization of the cooling fin distribution. Maduabuchi (2022) shows the use of deep learning network techniques trained through ANSYS simulations for parametric optimization of thermoelectrical for faster calculations using power, efficiency, and induced stresses as objectives.

The numerical implementation and performance of fully coupled thermo-electro-mechanical topology optimization remains largely unexplored compared to parametric analysis on these structures. Particularly, the SIMP method—widely adopted in structural optimization—has seen little application in this field. Despite the critical impact of stresses on device reliability and failure, the influence of optimization parameters on the resulting designs has not been studied in detail. Current optimization approaches for thermo-electro-mechanical problems lack sensitivity formulations to account for stress concentrations in these devices. Furthermore, existing studies rely on idealized fixed boundary conditions and neglect thermal losses to the environment, limiting the accuracy of the optimized designs.

This work presents a topology optimization framework for thermoelectric devices that incorporates mechanical stress considerations using the SIMP method, an approach not seen in the literature for this class of multiphysics problems. Unlike existing studies that focus solely on thermal and electrical behaviour, this method introduces mechanical degrees of freedom into the optimization process, enabling the inclusion of stress constraints critical to device reliability. We explore decoupled thermoelectrical and mechanical equations for the FEM simulations, examining their optimization convergence and optimized designs. A simplified model is proposed to simulate the electrical operating conditions of TECs using its voltage gradient across a thermocouple. We use this model to analyse the optimization results with and without stress constraints, addressing the impact of length scale on optimized designs through filtering techniques. We evaluate the effect of the results of Heaviside and Helmholtz filters and the need for filtering techniques due to the addition of stress constraints. This further contemplates studying the effect of grey regions in optimal thermo-electro-mechanical designs as opposed to pure thermoelectrical optimization. The examples consider both vacuum and air-filled environments to capture realistic thermal losses during operation. Prior work shows that air conduction dominates, while convection is negligible and radiation contributions depend on leg geometry with less than 10% effect for the device efficiency with leg gaps under 1 mm (Bjørk et al. 2014). A detailed study confirms the limited impact of radiation at low temperatures, particularly on power output rather than conversion efficiency Cai et al. (2020). Additionally, we present illustrative 2D and 3D results for a thermocouple under various constraint conditions, demonstrating convergence to lower semiconductor volumes with larger efficiencies and compliance compared to the initial design.

2 Governing equations

The physics of thermoelectric coolers in steady-state condition is governed by the thermoelectric coupling given by the electric charge and energy balance or equilibrium equations, i. e.,

$$\begin{aligned} &\nabla\cdot \mathbf{j} = 0, \\ &\nabla\cdot \mathbf{q} + \mathbf{j}\cdot\nabla\phi = q_\Omega. \end{aligned} \tag{1}$$

In these equations, we find the balance of current density $\mathbf{j}$ and heat flow $\mathbf{q}$ within our material depending on the applied electric field ϕ and the internal heat generation q_Ω. Furthermore, to study the induced stress, we also need to consider the mechanical static equilibrium

$$\nabla\cdot \boldsymbol{\sigma} + \mathbf{b} = \mathbf{0}, \tag{2}$$

with $\boldsymbol{\sigma}$ being the Cauchy stress tensor, $\mathbf{b}$ the body forces.

The constitutive equations in this problem rely on Ohm's equation, i. e.,

$$\mathbf{j} = -\gamma(\nabla\phi + \alpha\nabla T)\,. \tag{3}$$

This equation relates the current density $\mathbf{j}$ with the electric potential ϕ, the electrical conductivity γ, with the thermoelectric coupling to the temperature field T, through the Seebeck coefficient α. The coupling of the thermoelectric equations also involves Fourier's equation

$$\mathbf{q} = \alpha T\mathbf{j} - \kappa\nabla T\,, \tag{4}$$

which represents the contributions to the total energy flow of the current flow and the heat conduction. From Eq. (4), we see that the thermal conduction term depends on the temperature gradient and thermal conductivity κ, while the heat due to the current flow depends on the Seebeck coupling and current flow. Finally, the generalized Hooke equation or the isotropic linear thermoelastic constitutive equation for small displacements assumption in a 2D plane stress situation using the Voigt notation is

$$\hat{\boldsymbol{\sigma}} = \mathbf{C}\boldsymbol{\epsilon} - \boldsymbol{\beta}_T\theta\,, \tag{5}$$

$$\theta = (T - T_{\mathrm{ref}})\,, \tag{6}$$

$$\boldsymbol{\beta}_T = \frac{E}{1-2\nu}\left[\,1\;\;1\quad 0\,\right]^{\mathsf{T}}\alpha_T = \mathbf{C}\mathbf{e}_{\mathrm{tr}}\alpha_T, \quad , \tag{7}$$

where the isotropic coefficient of expansion α_T affects the normal stresses through a trace operator **e**. This equation relates the stresses with the material properties considering the thermoelastic problem where we define E as the Young's modulus of the material, and ν the Poisson's ratio, the reference temperature T_{ref}, the temperature at which there are no thermally induced stresses, $\boldsymbol{\epsilon}$ is the strains tensor, and **C** is the constitutive relation between the mechanical strain and stresses without thermal stresses. In a 2D plane stress problem, we define this constitutive relation as

$$\mathbf{C} = E\mathbf{C}_0 = \frac{E}{1-\nu^2}\begin{bmatrix} 1 & \nu & 0 \\ \nu & 1 & 0 \\ 0 & 0 & \frac{1-\nu}{2} \end{bmatrix}.$$

The strong form of the problem is completed by the boundary conditions

$$\begin{array}{lll} V = V_\Gamma \text{ on } \Gamma_V & T = T_\Gamma \text{ on } \Gamma_T & \boldsymbol{U_p} = \boldsymbol{U}_\Gamma \text{ on } \Gamma_U \\ \mathbf{j}\cdot\mathbf{n} = j_c \text{ on } \Gamma_j & \mathbf{q}\cdot\mathbf{n} = q_c \text{ on } \Gamma_q & \boldsymbol{\sigma}\cdot\mathbf{n} = \boldsymbol{t}_c \text{ on } \Gamma_t. \end{array} \tag{8}$$

In these boundary conditions, we impose fixed DOFs in the form of voltages V_Γ, temperatures T_Γ, and displacements $\boldsymbol{U}_\Gamma$, and external loads along their respective boundaries Γ_V, Γ_T , and Γ_U. The boundaries that prescribe primal and dual variables must be disjoint, i. e., , $\Gamma = \Gamma_V \,\bar{\cup}\, \Gamma_j$ and $\Gamma_V \cap \Gamma_j = \emptyset$ for the electrical problem. Similarly, for the thermal problem, we have $\Gamma = \Gamma_T \,\bar{\cup}\, \Gamma_q$ and $\Gamma_T \cap \Gamma_q = \emptyset$ and for the mechanical equilibrium $\Gamma = \Gamma_U \,\bar{\cup}\, \Gamma_t$ and $\Gamma_U \cap \Gamma_t = \emptyset$.

We approach the nonlinear thermoelectric problem previously presented through numerical procedures to overcome the challenge posed by an analytical solution.

2.1 Finite element modelling

To solve the coupled thermo-electro-mechanical through FEM, we reformulate the equations in weak form and discretize them by approximation functions. Using the residual, Garlekin's, and the divergence theorems, we get

$$\begin{aligned} &-\int_\Omega \omega\,\boldsymbol{\nabla}\cdot\mathbf{q}\,\mathrm{d}\Omega + \int_\Omega \omega\mathbf{j}\cdot\boldsymbol{\nabla}\phi\,\mathrm{d}\Omega + \int_{\Gamma_q} \omega q_c\,\mathrm{d}\Gamma \\ &\qquad = \int_\Omega \omega q_\Omega\,\mathrm{d}\Omega, \\ &-\int_\Omega \boldsymbol{\nabla}\omega\cdot\mathbf{j}\,\mathrm{d}\Omega + \int_{\Gamma_j} \omega\cdot\mathbf{j_c}\,\mathrm{d}\Gamma = 0, \\ &\int_\Gamma \omega\cdot\boldsymbol{\sigma}\,\mathrm{d}\Gamma - \int_\Omega \boldsymbol{\sigma}\cdot\boldsymbol{\nabla}\omega = 0, \end{aligned} \tag{9}$$

where ω is the weight function.

To discretize the weak forms in Eq. (9), we use standard bilinear shape functions. For the thermoelectric problem, temperature T and electric potential ϕ are interpolated using **N**. For the mechanical problem, the displacement field $\boldsymbol{U_p}$ is interpolated using $\mathbf{N_U}$. All these vectors are represented in column form. This interpolation is written as

$$T = \mathbf{N}^{\mathsf{T}}\mathbf{t},\ \phi = \mathbf{N}^{\mathsf{T}}\mathbf{v},\ \boldsymbol{U_p} = \mathbf{N_U}^{\mathsf{T}}\mathbf{u},\ \theta = \mathbf{N}^{\mathsf{T}}\left(\boldsymbol{t} - \boldsymbol{T}_{\mathrm{ref}}\right), \tag{10}$$

where vectors **t**, **v** , and **u** are the temperature, electric potential, and displacement DOFs at element level, respectively. We use these shape functions and discretized displacements to define strain–displacement matrix **B** as

$$\boldsymbol{\varepsilon} = \mathbf{B}\,\mathbf{u}. \tag{11}$$

The strain–displacement matrix can be introduced into the mechanical weak-form equation and using the Hooke thermoelastic relation, Eq. (5), to obtain the residual from the mechanical coupling $\mathbf{r_u}$

$$\begin{aligned} \mathbf{r_u} &= \int_\Gamma \mathbf{N_U}^{\mathsf{T}}\boldsymbol{\sigma}\,\mathbf{d}\Gamma - \mathbf{k_u}\mathbf{u} + \mathbf{k_\Theta}\boldsymbol{\theta} = \mathbf{0}, \\ \mathbf{k_u} &= \int_\Omega \mathbf{B}^{\mathsf{T}}\mathbf{C}\mathbf{B}\,\mathbf{d}\Omega, \\ \mathbf{k_\Theta} &= \int_\Omega \mathbf{B}^{\mathsf{T}}\boldsymbol{\beta}_T\mathbf{N}^{\mathsf{T}}\,\mathbf{d}\Omega. \end{aligned} \tag{12}$$

The residuals of the remaining thermoelectrical coupling given by Eq. (9) are

$$\begin{aligned} \mathbf{r_t} &= -\int_\Omega \mathbf{N}\,\boldsymbol{\nabla}\cdot\mathbf{q}\,\mathbf{d}\Omega + \int_\Omega \mathbf{N}\mathbf{j}\cdot\boldsymbol{\nabla}\mathbf{N}^{\mathsf{T}}\mathbf{v}\,\mathbf{d}\Omega + \\ &\quad \int_{\Gamma_q} \mathbf{N}q_c\,\mathbf{d}\Gamma - \int_\Omega \mathbf{N}q_\Omega\,\mathbf{d}\Omega = \mathbf{0}, \\ \mathbf{r_v} &= -\int_\Omega \boldsymbol{\nabla}\mathbf{N}\cdot\mathbf{j}\,\mathbf{d}\Omega + \int_{\Gamma_j} \mathbf{N}\cdot\mathbf{j_c}\,\mathbf{d}\Gamma = \mathbf{0}. \end{aligned} \tag{13}$$

The residual and element level state vectors are assembled into

$$\begin{aligned} &\mathbf{r} = \left[\,\mathbf{r_u}\;\mathbf{r_t}\;\mathbf{r_v}\,\right]^{\mathsf{T}} \text{ and} \\ &\mathbf{s} = \left[\,\mathbf{u}\;\mathbf{t}\;\mathbf{v}\,\right]^{\mathsf{T}}. \end{aligned} \tag{14}$$

The derivative of this residual concerning the unknown DOFs is tangent matrix **K**. Considering the null derivatives of the residual, this matrix can be written at the element level as

$$\mathbf{k}^{(k)} = \frac{\mathrm{d}\mathbf{r}}{\mathrm{d}\mathbf{s}} = \begin{bmatrix} \frac{\partial\mathbf{r}_\mathbf{u}^{(k)}}{\partial\mathbf{u}} & \frac{\partial\mathbf{r}_\mathbf{u}^{(k)}}{\partial\mathbf{t}} & \mathbf{0} \\ \mathbf{0} & \frac{\partial\mathbf{r}_\mathbf{t}^{(k)}}{\partial\mathbf{t}} & \frac{\partial\mathbf{r}_\mathbf{t}^{(k)}}{\partial\mathbf{v}} \\ \mathbf{0} & \frac{\partial\mathbf{r}_\mathbf{v}^{(k)}}{\partial\mathbf{t}} & \frac{\partial\mathbf{r}_\mathbf{v}^{(k)}}{\partial\mathbf{v}} \end{bmatrix}, \tag{15}$$

where the development of each derivative of the residual can be found in Appendix A. The global stiffness matrix can be obtained through the standard FEM assembly procedure

$$\mathbf{K}^{(k)} = \frac{\mathrm{d}\mathbf{R}^{(k)}}{\mathrm{d}\mathbf{S}} = \sum_{e=1}^{n_e} \mathbf{k}^{(k)}, \tag{16}$$

with **R** and **S** the global residual and state vectors arising from the assembly of **k** and for all elements e.

From the definition in Eq. (15), we see that the thermoelectrical DOFs are decoupled from the mechanical DOFs **u**. This decoupling allows us to use the reduced thermoelectrical tangent stiffness

$$\mathbf{K}_{\mathbf{TV}}^{(k)} = \begin{bmatrix} \frac{\partial \mathbf{R}_{\mathbf{T}}^{(k)}}{\partial \mathbf{T}} & \frac{\partial \mathbf{R}_{\mathbf{T}}^{(k)}}{\partial \mathbf{V}} \\ \frac{\partial \mathbf{R}_{\mathbf{V}}^{(k)}}{\partial \mathbf{T}} & \frac{\partial \mathbf{R}_{\mathbf{V}}^{(k)}}{\partial \mathbf{V}} \end{bmatrix}, \tag{17}$$

to compute the global thermal and electrical DOFs $\begin{bmatrix} \mathbf{T} & \mathbf{V} \end{bmatrix}$ using the Newton–Raphson method, starting with $\begin{bmatrix} \mathbf{T} & \mathbf{V} \end{bmatrix} = \mathbf{0}$ as an initial solution. Each system is solved using MATLAB's direct sparse linear solver. Subsequently, global displacements **U** are determined in a second step, incorporating the computed temperature field into the thermoelastic equation Eq. (12). Notably, the solution step of the thermoelastic equation is only nonlinear in scenarios featuring the temperature-dependent Young's modulus or the coefficient of thermal expansion.

To validate the MATLAB implementation, a test routine was developed using analytical benchmarks from Pérez-Aparicio et al. (2007), supplemented with analytically calculated thermoelastic deformations. Matrix dimensions and implementation details are provided in Appendix A. For a fully coupled FEM formulation including thermoelectricity, displacement, and magnetic flux, see Pérez-Aparicio et al. (2016).

3 Problem formulation

With the finite element formulation of the coupled thermo-electro-mechanical problem in place, we define our design optimization procedure. We use a density-based TO formulation, following the three-field-density formulation from Lazarov et al. (2016). In this material representation, we use three density fields $(\bar{\boldsymbol{x}}_\rho, \widetilde{\boldsymbol{x}}_\rho, \boldsymbol{x}_\rho)$. Each one represents the density design variables used by the optimizer $\boldsymbol{x}_\rho$, the filtered density design variables $\widetilde{\boldsymbol{x}}_\rho$, and the physical density design variables $\bar{\mathbf{x}}_\rho$.

The filtered density field is obtained through the Helmholtz equation Lazarov and Sigmund (2011)

$$-d_r^2 \nabla^2 \widetilde{x}_\rho + \widetilde{x}_\rho = x_\rho, \tag{18}$$

where $\widetilde{x}_\rho$ and x_ρ represent filtered density design variables and the density variables used by MMA at element level. In the equation, d_r is a characteristic radius that introduces a length scale in the optimization.

We discretize the Helmholtz equation using standard linear interpolation functions $\mathbf{N}_h$ at the element level, based on standard 8-node hexahedral elements (in 3D) or 4-node quadrilateral elements (in 2D). We use the relation $x_\rho = \mathbf{N}_h^{\mathrm{T}} \boldsymbol{x}_e$ and $\widetilde{x}_\rho = \mathbf{N}_h^{\mathrm{T}} \widetilde{\boldsymbol{x}}_e$. In these relations, $\boldsymbol{x}_e$ and $\widetilde{\boldsymbol{x}}_e$ are the nodal density values for each field at element level. The discretized Helmholtz equation is written as

$$\begin{aligned} &-\int \mathbf{N}_h d_r^2 \nabla^2 (\mathbf{N}_h^{\mathrm{T}} \widetilde{\boldsymbol{x}}_e) \mathbf{d}\Omega + \int \mathbf{N}_h \mathbf{N}_h^{\mathrm{T}} \widetilde{\boldsymbol{x}}_e \mathbf{d}\Omega \\ &= \int \mathbf{N}_h^{\mathrm{T}} \boldsymbol{x}_e \mathbf{d}\Omega\,. \end{aligned} \tag{19}$$

Applying the divergence theorem and Neumann boundary conditions, we obtain

$$\int \nabla \mathbf{N}_h d_r^2 \nabla (\mathbf{N}_h^{\mathrm{T}} \widetilde{x}_e) \mathbf{d}\Omega + \int \mathbf{N}_h \mathbf{N}_h^{\mathrm{T}} \widetilde{x}_e d\Omega = \int \mathbf{N}_h^{\mathrm{T}} x_e \mathbf{d}\Omega. \tag{20}$$

We can write the previous equation as a system of linear equations using a filtering stiffness matrix $\mathbf{K}_h$ using our design variables $\boldsymbol{x}_\rho$ and an assembly procedure, i.e.

$$\begin{aligned} &\mathbf{K}_h \widetilde{\boldsymbol{x}}_\rho = \mathbf{H} \boldsymbol{x}_\rho, \quad \text{where} \\ &\mathbf{K}_h = \sum_{e}^{n_e} \left(\int \left(\nabla \mathbf{N}_h^{\mathrm{T}} d_r^2 \nabla \mathbf{N}_h + \mathbf{N}_h^{\mathrm{T}} \mathbf{N}_h \right) \mathbf{d}\Omega \right). \end{aligned} \tag{21}$$

In this formulation, **H** is a matrix whose column i contains the element level integration $\int \mathbf{N}_h d\Omega$ for the nodes of the element $e == i$.

The preconditioned conjugate gradients method provides the solution to this system. As this $\mathbf{K}_h$ matrix only depends on the mesh, we use a single preconditioning and store it throughout the optimization procedure, reducing the computational cost of filtering the design space Lundgaard and Sigmund (2018). Finally, to recover the element density after filtering, we use the approximation function for the centroid of each element $\mathbf{N}_h(0,0,0)$.

To provide a sharp change between void and solid material, we apply a Heaviside projection to the filtered design that provides the physical density design variable

$$\bar{x}_\rho = \frac{\tanh(\beta\mu) + \tanh\left(\beta(\widetilde{x}_\rho - \mu)\right)}{\tanh(\beta\mu) + \tanh\left(\beta(1-\mu)\right)}. \tag{22}$$

The β variable determines the sharpness of the projection and μ the step location.

The physical density design variable provides the relation

$$\rho_e = \bar{x}_\rho \rho_s, \tag{23}$$

where the physical density design variable of the e-th design element is directly related to the density of the eth element ρ_e, with respect to its solid density ρ_s.

The rest of the material properties can be written for each element using a power law following a modified SIMP approach (Bendsøe and Kikuchi 1988; Rozvany et al. 1992), as follows:

$$\begin{aligned} \alpha &= \alpha_v + \bar{x}_\rho^{p_\alpha}(\alpha_s(T) - \alpha_v), \\ \kappa &= \kappa_v + \bar{x}_\rho^{p_\kappa}(\kappa_s(T) - \kappa_v), \\ \gamma &= \gamma_v + \bar{x}_\rho^{p_\gamma}(\gamma_s(T) - \gamma_v), \\ E &= E_v + \bar{x}_\rho^{p_E}\left(E_s(T) - E_v\right). \end{aligned} \tag{24}$$

The properties of the solid material are indicated by the subscript $\square_s$ in Eq. (24), and we define them according to experimental data. Minimum material properties for void elements are imposed to avoid the singularity in the tangent matrices with a user-defined value $\square_v$. p_S, p_κ, p_γ , and p_E are the penalization coefficients for their corresponding material property. Intermediary densities in the optimal design are equivalent to non-manufacturable porous materials. For this reason, the penalization coefficient tries to ensure the optimized results lead to a fully black-and-white design.

Furthermore, we use nonlinear temperature-dependent properties for each material. We modelled the properties of the semiconductors following the measurements for Bi_2Te_3 by Witting et al. (2019), using the lowest doping values for each semiconductor. The provided values are fitted to a continuous polynomial as detailed in Appendix C within the measured temperature range. We enforce constant material properties for temperatures outside of this range. If the outcome from the optimization falls within this constant material property range, their results should be reevaluated, or the material properties extended to accommodate a broader range. In addition to semiconductor material, we need to define the properties of copper for electrical terminals, aluminium nitride (AlN) for the thermal ceramic contacts, and SAC 305 (tin-silver-copper) as solder. These material properties are kept constant with temperature to avoid further nonlinearities in the optimization procedure. We summarize all temperature-constant material properties used in this model in Table 7.

3.1 Topology optimization formulation

With the density design variables and filtering techniques established, we need to define the optimization problem that will guide the design variables. We can define this problem for cooling applications through a temperature-based objective, power constraints, and voltage design variables to limit the electrical working point, stress constraints for reliability, and volume fraction limits to reduce costs. We can describe this formulation as

$$\mathbf{x}^*_{\boldsymbol{\Phi}} = \underset{\mathbf{x}_{\boldsymbol{\Phi}}}{\arg\min} \qquad \boldsymbol{\Phi} = \Psi\left(\mathbf{T}_{\boldsymbol{\Phi}}\right), \tag{25a}$$

$$\text{such that} \qquad c_\sigma = \Psi\left(\frac{\sigma_{VM}}{\sigma_0}\right) - 1 \leq 0, \tag{25b}$$

$$c_P = \frac{P}{P_0} - 1 \leq 0, \tag{25c}$$

$$c_v = \sum_{e=1}^{n_e} \frac{v_e x_\rho}{v_0 v_{\text{obj}}} - 1 \leq 0, \tag{25d}$$

$$V_\Gamma = V_{\min} + x_S(V_{\max} - V_{\min}), \tag{25e}$$

$$\mathbf{R} = \mathbf{0}, \tag{25f}$$

where we look for the design variables $\boldsymbol{x}_{\boldsymbol{\Phi}}$ that minimize an objective function $\boldsymbol{\Phi}$ submitted to several constraints. For this optimization, we define a vector of design variables $\mathbf{x}_{\boldsymbol{\Phi}} = \left[\boldsymbol{x}_\rho \ \boldsymbol{x}_S\right]^\intercal$, containing the density design variables $\boldsymbol{x}_\rho$ and the design variables controlling the voltage Dirichlet imposed boundary conditions $\boldsymbol{x}_S$ which for our model can be reduced to a single boundary condition V_Γ between a given minimum and maximum voltages defined as $V_{\min}$ as $V_{\max}$. This allows us to take into account the optimum efficiency of thermocouples with respect to the current flow across the device for all geometries, which is a nonlinear effect. The overall objective of our optimization is then the temperature of our heat injection surface, considering a power limit and controlling the power consumption of the system. Furthermore, we limit the stresses at which the device is submitted and incorporate a volume constraint to reduce semiconductor material volume and associated costs. The objective function depends on a temperature field $\mathbf{T}_{\boldsymbol{\Phi}}$ on $\Gamma_{\boldsymbol{\Phi}}$ and an aggregation function Ψ. The problem is subjected to various constraints, including a stress constraint c_σ, a power constraint c_P , and a volume constraint c_v. The stress constraint is based on limiting stress σ_0 and a field of von Misses stresses aggregated through the same function as the objective function. The power constraint requires a ratio between the overall power consumption of the device P and a limit power P_0. The volume constraint depends on the summation of the volume of each element v_e compared to the total volume of the original design v_0 and a limiting volume v_{obj}.

As aggregation function Ψ, we use the P-mean, which increases the influence on the function of the values that deviate most from the mean of the input values using a penalization factor p_Ψ. The P-mean is defined as

$$\Psi(\mathbf{f}) = \left(\frac{1}{n_i} \sum_{i=1}^{n_i} f_i^{p_\Psi} \right)^{\frac{1}{p_\Psi}}, \tag{26}$$

with $\mathbf{f}$ a vector field and n_i its size. Ψ provides a lower-bound of the maximum value stored in $\mathbf{f}$,

$$\Psi(\mathbf{f}) \leq \max(f_1, f_2, \ldots, f_{n_i}), \tag{27}$$

leading to an underpenalization of the constraints or maximum values in the field Fernández et al. (2019). This function has an asymptotic behaviour towards the maximum in the distribution with increasing p_Ψ values (Verbart et al. 2017). This means its behaviour will also lead to higher nonlinearities, the larger the penalization coefficient p_Ψ. The stress constraint and the objective functions use this formulation to avoid stress concentrations and hot spots in the optimized designs. The values used within the exponential aggregation function must be rescaled to values close to unity to avoid singularities in the numerical calculation. This can be done in each case through a reference temperature, where we use the initial device temperature of 25°C, and the limiting stress σ_0.

We also rescale the other constraints to maximum values between 1 and 100 using the objective volume and power to improve the convergence of the MMA optimizer (Svanberg 2014). This algorithm, proposed by Svanberg (1987), uses a local convex approximation function in successive iterations to find local minima. MMA has been repeatedly tested in TO problems with success in finding minima. The stopping criteria of the algorithm used is based on a total number of iterations or the relative change between the design variables $\bar{\mathbf{x}_\Phi}$,

$$\begin{aligned} &\text{Stop if} \quad \frac{1}{\dim(\bar{\mathbf{x}}_{\boldsymbol{\Phi}})} \left\| \left(\bar{\mathbf{x}}_{\boldsymbol{\Phi}}^{(i-2)} - \bar{\mathbf{x}}_{\boldsymbol{\Phi}}^{(i)} \right) \oslash \bar{\mathbf{x}}_{\boldsymbol{\Phi}}^{(i)} \right\|_2 < \varepsilon_{\mathrm{KKT}} \\ &\text{or} \qquad\qquad\qquad\qquad\qquad\qquad\qquad\qquad\qquad i \geq i_{\max}. \end{aligned}$$

Because MMA is a gradient descent algorithm, we must formulate the sensitivities for the objective and constraint functions.

3.2 Sensitivity calculation

To apply a gradient-based optimization algorithm, we need analytical expressions for the sensitivities of each objective and constraint function concerning the design variables and validate them against finite differences methods according to Appendix B. We calculate these sensitivities for the filtered field, $\bar{\boldsymbol{x}}_{\boldsymbol{\Phi}} = \left[\bar{x}_\rho \;\; x_S \right]^\intercal$, although these can be easily extended to any number of boundary condition control variables. Given the use of $\boldsymbol{x}_\rho$ by the optimizer and the $\bar{\boldsymbol{x}}_\rho$ by our FEM, to recover the sensitivities of a function ψ, with respect to the density design variables, we need to follow the chain rule

$$\frac{\partial \psi}{\partial \boldsymbol{x}_\rho} = \frac{\partial \psi}{\partial \bar{\boldsymbol{x}}_\rho} \cdot \frac{\partial \bar{\boldsymbol{x}}_\rho}{\partial \widetilde{\boldsymbol{x}}_\rho} \cdot \frac{\partial \widetilde{\boldsymbol{x}}_\rho}{\partial \boldsymbol{x}_\rho}. \tag{28}$$

We can express the derivative of the filtered design space relative to the density values as

$$\frac{\partial \widetilde{\boldsymbol{x}}_\rho}{\partial \boldsymbol{x}_\rho} = \mathbf{K}_h^{-1} \mathbf{H}. \tag{29}$$

We can recalculate the result of the modified sensitivities through the vector containing the sensitivities to the filtered design variables and a single calculation using the conjugate gradients method. The nodal sensitivities can then be recovered as the mean of each element, as we do for the filtered densities.

The derivative of the physical field concerning the filtered field is given by

$$\frac{\partial \bar{x}_\rho}{\partial \widetilde{x}_\rho} = \frac{\beta \left(\tanh^2 \left(\beta(\mu - \widetilde{x}_\rho) \right) - 1 \right)}{\tanh \left(\beta(\mu - 1) \right) - \tanh(\beta \mu)}. \tag{30}$$

The sensitivities with respect to the physical density field are then solved through the *adjoint method* through the definition of the Lagrangian

$$L = \boldsymbol{\psi} + \boldsymbol{\Lambda}^\intercal \mathbf{R}. \tag{31}$$

In this definition, L represents the Lagrangian, $\boldsymbol{\Lambda}$ is the adjoint vector, and ψ is the objective or constraint function. The general solution to the total derivative of any Lagrangian functional can be solved through the definition of a $\boldsymbol{\Lambda}$ constant vector that removes from the equation the derivative of the state vector $\mathbf{S}$ concerning our design variables $\boldsymbol{x}$. The general equation that solves $\boldsymbol{\Lambda}$ looks like

$$-\left(\frac{\partial \mathbf{R}}{\partial \mathbf{S}} \right)^\intercal \boldsymbol{\Lambda} = \left(\frac{\partial \psi}{\partial \mathbf{S}} \right)^\intercal. \tag{32}$$

Given that the first component of the equation is the tangent stiffness matrix, we can decompose this calculation as we do for the Newton-Raphson iterative procedure, reducing memory allocation. The solution can then be the following 2 steps:

$$-\left(\frac{\partial \mathbf{R}_{\mathbf{U}}}{\partial \mathbf{U}} \right)^\intercal \boldsymbol{\Lambda}_U = \left(\frac{\partial \psi}{\partial \mathbf{U}} \right)^\intercal, \tag{33}$$

$$-\left(\mathbf{K}_{\mathbf{TV}} \right)^\intercal \boldsymbol{\Lambda}_{TV} = \left[\tfrac{\partial \psi}{\partial \mathbf{T}} \;\; \tfrac{\partial \psi}{\partial \mathbf{V}} \right]^\intercal + \left(\frac{\partial \mathbf{R}_U}{\partial \mathbf{T}} \right)^\intercal \boldsymbol{\Lambda}_U. \tag{34}$$

In the previous separation of the mechanical and thermoelectric solutions of the adjoint vector, we separate it as

$$\boldsymbol{\Lambda}^\intercal = \left[\boldsymbol{\Lambda}_{\mathbf{U}} \;\; \boldsymbol{\Lambda}_{\mathbf{T}} \;\; \boldsymbol{\Lambda}_{\mathbf{V}} \right] = \left[\boldsymbol{\Lambda}_{\mathbf{U}} \;\; \boldsymbol{\Lambda}_{\mathbf{TV}} \right]. \tag{35}$$

Substituting these solutions into the Lagrangian derivative, we can calculate the derivatives of the function ψ as

$$\frac{\mathrm{d}L}{\mathrm{d}\bar{\boldsymbol{x}}_{\boldsymbol{\Phi}}} = \frac{\mathrm{d}\psi}{\mathrm{d}\bar{\boldsymbol{x}}_{\boldsymbol{\Phi}}} = \frac{\partial\psi}{\partial\bar{\boldsymbol{x}}_{\boldsymbol{\Phi}}} + \boldsymbol{\Lambda}^{\intercal}\left(\frac{\partial\mathbf{R}}{\partial\bar{\boldsymbol{x}}_{\boldsymbol{\Phi}}}\right). \tag{36}$$

This solution still requires the derivative of the residual and the function ψ concerning each design variable in $\boldsymbol{x}$. This $\bar{\boldsymbol{x}}_{\boldsymbol{\Phi}}$ comprises filtered density design variables and boundary condition control variables. We can identify two different cases. In the case of the derivatives concerning a density variable $\bar{x}_\rho$, the calculation can be taken to the element level as

$$\frac{\mathrm{d}\psi}{\mathrm{d}\bar{x}_\rho} = \frac{\partial\psi}{\partial\bar{x}_\rho} + \boldsymbol{\Lambda}_e^{\intercal}\left(\frac{\partial\mathbf{r}}{\partial\bar{x}_\rho}\right). \tag{37}$$

In the previous equation, $\boldsymbol{\Lambda}_e$ represents the adjoint solution for the DOFs associated with element e and $\bar{x}_\rho$ its associated density design variable. The second case refers to the sensitivity concerning a boundary condition. In this case, we can use the chain rule as

$$\frac{\mathrm{d}\psi}{\mathrm{d}x_S} = \frac{\partial\psi}{\partial\mathbf{S}}\frac{\partial\mathbf{S}}{\partial S_\Gamma}\frac{\partial S_\Gamma}{\partial x_S} - \boldsymbol{\Lambda}^{\intercal}\left(\frac{\partial\mathbf{R}}{\partial\mathbf{S}}\frac{\partial\mathbf{S}}{\partial S_\Gamma}\frac{\partial S_\Gamma}{\partial x_S}\right). \tag{38}$$

In this equation, we require the derivative of ψ concerning the state vector, already calculated for the adjoint vector system. Now, we need to define the derivative of the state vector concerning the fixed value used in our boundary condition S_Γ. While this is a general formulation that can be applied to Dirichlet boundary conditions in U, T or V as expressed in Eq. (8), we particularize it for a voltage boundary condition V_Γ as

$$\frac{\partial\mathbf{U}}{\partial V_\Gamma} = \mathbf{0}, \tag{39}$$

$$\frac{\partial\mathbf{T}}{\partial V_\Gamma} = \mathbf{0}, \tag{40}$$

$$\frac{\partial V_i}{\partial V_\Gamma} = \begin{cases} 1 & \text{if } \mathbf{x}(i) \in \Gamma_V; \\ 0 & \text{otherwise,} \end{cases} \tag{41}$$

where Γ_V is the location of the boundary condition we control through x_S and $\mathbf{x}$ is the coordinates of node i.

The last component needed is the derivative of the value associated with the boundary condition concerning its control variable following the description in Eq. (25e). The derivative of the voltage boundary condition concerning the control variable can be expressed as

$$\frac{\partial V_\Gamma}{\partial x_S} = V_{\max} - V_{\min}, \tag{42}$$

where $V_{\max}$ and $V_{\min}$ define the minimum and maximum voltage that we apply across our thermoelectrical device.

Given the previous formulation, the derivative of the ψ function with respect to a design variable controlling boundary condition is nonzero only if the domain affected by the constraint or objective ψ includes the nodes associated with that boundary condition. We can state this fact for our voltage boundary condition as

$$\frac{\partial\psi}{\partial\mathbf{S}}\frac{\partial\mathbf{S}}{\partial V_\Gamma} = \frac{\partial\psi}{\partial V_\Gamma} = 0 \text{ if } \Gamma_\psi \cap \Gamma_V = \emptyset, \tag{43}$$

where Γ_ψ are the DOFs used by ψ.

These equations provide all the quantities that need to be defined to calculate for each objective and constraint. In the following subsections, we provide the derivatives of each ψ function with respect to S and $\bar{\boldsymbol{x}}_{\boldsymbol{\Phi}}$. The common derivatives for all functions of $\mathbf{r}$ and material properties are provided in the Appendix A.

3.2.1 Objective function

We use the P-mean of the nodal temperature values in the cold surface of the thermocouple as our objective, $\Gamma_{\boldsymbol{\Phi}}$. This equation is written in Eq. (25).

To calculate its derivative with respect to the state vector, we can rewrite it in terms of the of all DOFs using a vector $\mathbf{L}_{\boldsymbol{\Phi}}$ which stores the components of $\mathbf{T}$ present in $\boldsymbol{\Gamma}_{\boldsymbol{\Phi}}$ and performs the division concerning the number of elements in the summation. This multiplier $\mathbf{L}_{\boldsymbol{\Phi}}$ contains

$$\mathbf{L}_{\boldsymbol{\Phi}}(i) = \begin{cases} \frac{1}{n_{\boldsymbol{\Phi}}} & \text{if } \mathbf{x}(i) \in \Gamma_{\boldsymbol{\Phi}}; \\ 0 & \text{otherwise.} \end{cases}, \tag{44}$$

where $n_{\boldsymbol{\Phi}}$ is the number of DOFs used to summate the P-mean function and $\mathbf{x}$ are the coordinates of node i. The objective function can then be written as

$$\Psi(\mathbf{T}_{\boldsymbol{\Phi}}) = \left(\mathbf{L}_{\boldsymbol{\Phi}}^{\intercal}\mathbf{T}^{\circ p_\Psi}\right)^{\frac{1}{p_\Psi}}. \tag{45}$$

The derivative of this objective with respect to the global temperature DOFs can now be written as

$$\frac{\partial\boldsymbol{\Phi}}{\partial\mathbf{T}} = \mathbf{L}_{\boldsymbol{\Phi}}\circ\mathbf{T}^{\circ(p_\Phi-1)}\left(\mathbf{L}_{\boldsymbol{\Phi}}^{\intercal}\mathbf{T}^{\circ p_\Phi}\right)^{\left(\frac{1}{p_\Phi}-1\right)}. \tag{46}$$

This can be rewritten in terms of the global state vector $\mathbf{S}$ as

$$\frac{\partial\boldsymbol{\Phi}}{\partial\mathbf{S}} = \begin{bmatrix} \frac{\partial\boldsymbol{\Phi}}{\partial\mathbf{U}} \\ \frac{\partial\boldsymbol{\Phi}}{\partial\mathbf{T}} \\ \frac{\partial\boldsymbol{\Phi}}{\partial\mathbf{V}} \end{bmatrix} = \begin{bmatrix} \mathbf{0} \\ \frac{\partial\boldsymbol{\Phi}}{\partial\mathbf{T}} \\ \mathbf{0} \end{bmatrix}. \tag{47}$$

The partial derivative of the objective function with respect to any density design variable is zero

$$\frac{\partial \boldsymbol{\Phi}}{\partial \bar{\mathbf{x}}_\rho} = \mathbf{0}\,. \tag{48}$$

Notice that these equations do not depend on the mechanical DOFs. Therefore, the two-step adjoint equation calculation can be simplified with

$$\boldsymbol{\Lambda}_U = \mathbf{0}. \tag{49}$$

3.2.2 Stress constraint

For each element, we consider a single $\hat{\boldsymbol{\sigma}}$ value calculated at its centroid—equivalent to a zero value for its local coordinates $\boldsymbol{\xi} = \mathbf{0}$. The space of these centroids makes up $\Gamma_{\boldsymbol{\Phi}}$. The centroid reference for the stresses provides an exact value for hexahedral serendipity elements (H20) without the need for extrapolation for Gauss integration schemes if $\boldsymbol{\xi} = \mathbf{0}$ is used as an integration point (Sharma 2016). The lack of extrapolation and use of a single evaluation point per element simplifies the calculation of this constraint at the cost of a lower number of evaluation points for the stress constraint. Given these assumptions, we can reduce the derivative of the von Misses stress with respect to each one of the stresses stored in the Voigt notation to the element level.

The partial derivative of the P-mean function of the stress within the design domain requires the calculation of a summation along all nodes n_σ included in the design domain. Following the chain rule, we have

$$\frac{\partial c_\sigma}{\partial \mathbf{S}} = k_\sigma \sum_{e=1}^{n_\sigma} \left(\left(\frac{\sigma_{VM}^{(e)}}{\sigma_0} \right)^{p_\Psi - 1} \begin{bmatrix} \frac{\partial \sigma_{VM}^{(e)}}{\partial \hat{\boldsymbol{\sigma}}} \frac{\partial \hat{\boldsymbol{\sigma}}}{\partial \mathbf{u}} \\ \frac{\partial \sigma_{VM}^{(e)}}{\partial \hat{\boldsymbol{\sigma}}} \frac{\partial \hat{\boldsymbol{\sigma}}}{\partial \mathbf{t}} \\ \frac{\partial \sigma_{VM}^{(e)}}{\partial \hat{\boldsymbol{\sigma}}} \frac{\partial \hat{\boldsymbol{\sigma}}}{\partial \mathbf{v}} \end{bmatrix} \right). \tag{50}$$

In this equation, we have a k_σ constant arising from the derivative of the P-mean function and defined as

$$k_\sigma = \frac{1}{n_\sigma \sigma_0} \left(\frac{1}{n_\sigma} \sum_{e=1}^{n_\sigma} \left(\frac{\sigma_{VM}^{(e)}}{\sigma_0} \right)^{p_\Psi} \right)^{\frac{1}{p_\Psi} - 1}. \tag{51}$$

Each derivative of a single von Misses stress value with respect to the local stresses is given by

$$\frac{\partial \sigma_{VM}^{(e)}}{\partial \hat{\boldsymbol{\sigma}}} = \frac{1}{2\sigma_{VM}^{(e)}} \begin{bmatrix} (2\sigma_x - \sigma_y - \sigma_z) \\ (2\sigma_y - \sigma_x - \sigma_z) \\ (2\sigma_z - \sigma_y - \sigma_x) \\ 6\tau_{yz} \\ 6\tau_{xz} \\ 6\tau_{xy} \end{bmatrix}^\intercal, \tag{52}$$

and the derivatives of the local stress vector with respect to the element level DOFs are

$$\frac{\partial \hat{\boldsymbol{\sigma}}}{\partial \mathbf{u}} = \mathbf{CB}, \tag{53}$$

$$\frac{\partial \hat{\boldsymbol{\sigma}}}{\partial \mathbf{t}} = \frac{\partial \mathbf{C}}{\partial T} \mathbf{BuN}^\intercal - \frac{\partial \beta_T}{\partial T} \boldsymbol{\theta} \mathbf{N}^\intercal - \beta_T \mathbf{N}^\intercal, \tag{54}$$

$$\frac{\partial \hat{\boldsymbol{\sigma}}}{\partial \mathbf{v}} = \mathbf{0}. \tag{55}$$

The derivative of the stress constraint with respect to the density design variables can be calculated at element is

$$\frac{\partial c_\sigma}{\partial \bar{\mathbf{x}}_\rho} = k_\sigma \left(\sum_{e=1}^{n_\sigma} \left(\frac{\sigma_{VM}^{(e)}}{\sigma_0} \right)^{p_\Psi - 1} \frac{\partial \sigma_{VM}^{(e)}}{\partial \hat{\boldsymbol{\sigma}}} \frac{\partial \hat{\boldsymbol{\sigma}}}{\partial \bar{x}_\rho} \right), \tag{56}$$

where the element level derivative of the Voigt notation stress of each element as

$$\frac{\partial \hat{\boldsymbol{\sigma}}}{\partial \bar{x}_\rho} = \frac{\partial \mathbf{C}}{\partial \bar{x}_\rho} \mathbf{Bu} - \frac{\partial \mathbf{C}}{\partial \bar{x}_\rho} \alpha_T \boldsymbol{\theta}, \tag{57}$$

3.2.3 Power constraint

We calculate the thermocouple power through the summation of the integration of the current density multiplied by the voltage gradient within each one of the elements in the mesh used for the power calculation n_P, i. e.,

$$P = \sum_{e=1}^{n_P} P_e = \sum_{e=1}^{n_P} \left(- \int_\Omega \mathbf{j}^\intercal \boldsymbol{\nabla} \mathbf{N}^\intercal \mathbf{v} \, \mathbf{d}\Omega \right). \tag{58}$$

The integral is performed at the element level, so the derivative can also be calculated at the element level and assembled through the summation of each element's component. The derivative of this function with respect to the state vector can be written as

$$\frac{\partial c_p}{\partial \mathbf{S}} = \frac{1}{P_0} \sum_{e=1}^{n_P} \int_\Omega \begin{bmatrix} \mathbf{0} \\ -\frac{\partial \mathbf{j}}{\partial \mathbf{t}}^\intercal \nabla \mathbf{N}^\intercal \mathbf{v} \\ -\frac{\partial \mathbf{j}}{\partial \mathbf{v}}^\intercal \nabla \mathbf{N}^\intercal \mathbf{v} - \nabla \mathbf{N} \mathbf{j} \end{bmatrix} d\Omega. \tag{59}$$

The derivative of the power with respect to the density design variables can also be reduced to element level as

$$\frac{\partial c_p}{\partial \bar{x}_\rho} = \frac{-1}{P_0} \int_\Omega \left(\frac{\partial \mathbf{j}}{\partial \bar{x}_\rho} \right)^\intercal \nabla \mathbf{N}^\intercal \mathbf{v} \, d\Omega. \tag{60}$$

The partial derivatives of the current density with respect to the density design variables and element level DOFs are provided in Appendix A.

As in the case of the temperature objective, the mechanical adjoint vector is zero. This can simplify the calculation of these derivatives.

3.2.4 Volume constraint

This constraint does not depend on the state vector or the boundary conditions, leading to the values:

$$\frac{\partial c_v}{\partial \mathbf{S}} = \mathbf{0}. \tag{61}$$

Nevertheless, this equation does depend on the element level densities

$$\frac{\partial c_v}{\partial \bar{x}_\rho} = \frac{v_e}{v_0 v_{\mathrm{obj}}}. \tag{62}$$

Given the previous equations, this solution does not require the calculation of the adjoint as the solution to the system Eq. (32) provides the trivial solution.

4 Results

This section provides examples of how we apply our formulation to the standard thermoelectrical element mechanical assembly. This is commonly done by introducing the TEC between two plates that can be tightened together using fasteners, adding a compression force into the thermoelectric device. These two plates act as cooling surfaces and heat sinks, respectively. After assembly, the entire thermocouple is under compression loading and cannot expand through its thickness.

4.1 2D results

Each TEC usually consists of multiple thermocouples, with each thermocouple being an in-series connection between dissimilar semiconductors. For our model, we simplify it to a single thermocouple, considering they are all submitted to the same loads. A 2*D* cross-section of a single thermocouple is depicted in Fig. 1. In this figure, we can appreciate a cross-section of the *yz* plane of a thermoelectrical pellet composed of a $p+$ and $n-$ semiconductor pellets joined together by a solder (white blocks) and a copper layer (solid grey blocks). Two ceramic layers (hatched blocks) act as the thermal contacts in this assembly. This figure also shows the boundary conditions at each of the outer edges. The mechanical boundary conditions include a zero displacement in the heat sink and cooling surface along the z axis to simulate the mechanical assembly and at the connection with the surrounding thermocouples with zero displacements along the ceramic and copper connections to the surrounding material in the x direction. The thermoelectrical model imposes a heat flux q_{in} at the cold surface of the TEC and a heat sink with a prescribed temperature T_0 on the opposite surface. Both these thermal boundary conditions are imposed in the ceramic layers. Electrical boundary conditions are applied to each copper electrode, i. e., a voltage $V_f > 0$ at one end and $V_0 = 0$ in the opposite one, according to the definition of the $p+$ and $n-$ materials. Reversing this definition would warm the objective surface instead of cooling it. Finally, as ceramic materials are not electrically conductive, we fix the voltage value of these solids to zero to avoid numerical instabilities. The nodes in contact between both solids, the copper and the ceramic layer, are not fixed and are solved in each iteration.

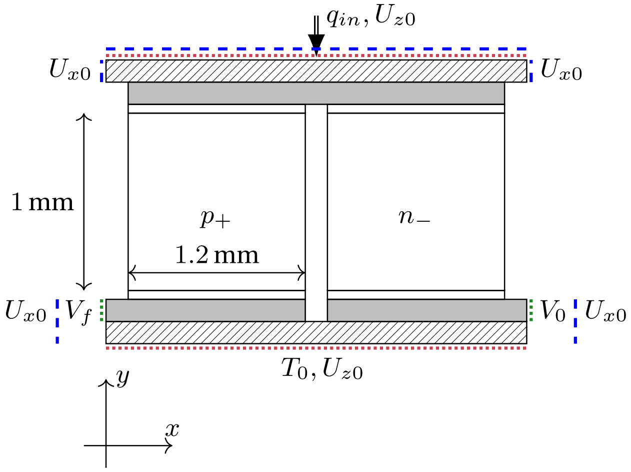

Fig. 1 Thermocouple FEM simplified model. The figure includes the heat injection q_{in} and temperature boundary conditions T_0 in red, voltages (V_0, V_f) in green, and displacements in blue U_{x0}. The different layers include a grey copper connection, a hashed ceramic layer, and two thermoelectrical pellets soldered to the copper through a solder layer

With our 2D model, we now set the optimization parameters. The TO computational domain within the design in Fig. 1 is set only to the thermoelectrical elements, i. e., Bi_2Te_3 material regions. While the copper, ceramic, and solder layers can impact the objective and constraint functions, we do not include their topology in the design space. We create the mesh of Bi_2Te_3 using a regular 60×60 grid, totalling 3600 serendipity 8-node elements (Q8) per semiconductor leg. The dimensions of the default thermoelectrical pellet are based on standard thermoelectrical devices and are equal to 1mm × 1.2mm. The solder, copper, and ceramic layers measure 0.05, 0.1, and 0.2mm, respectively, and the gap between two pellets is 0.2mm. We set the limits of the voltage gradient across the thermocouple defined by the x_S design variable to 0.01V and 0.06V and equal to V_f. The initial value imposed to x_S during the optimization is 0, providing the smallest voltage possible according to Eq. (25e).

For subsequent optimizations without any filtering scheme, we start from the full-density design, $\bar{\boldsymbol{x}}_{\boldsymbol{\Phi}} = \boldsymbol{x}_{\boldsymbol{\Phi}} = \mathbf{0.5}$, given the lack of information on a better initialization design and the need for a fully connected design. The minimum material property value for all materials according to Eq. (24) is set to 10^{-6} to avoid numerical instabilities. Furthermore, we fix the heat flux to $7500\ \mathrm{W/m^2}$ and the power consumption to 15mW per thermocouple. We can translate this power consumption limit for the $2D$ case to 15W/m, considering a thickness of 1 mm for the thermocouple. Finally, the MMA algorithm requires the definition of some parameters, including a hyperparameter c_m, to penalize the problem for infeasible design spaces. All c_m values are set to 20,000, and the optimization is run for a number of iterations i_m of 150. Notice that we obtain these values by trial and error, and if set too low, we might end up with an infeasible design. The penalization coefficient for each material property involved in the optimization has been selected by combinatorial analysis from an analytical model in Gutiérrez et al. (2024) to achieve convergence. For all optimizations, we use the set of penalization coefficients satisfying

$$p_S < p_k = p_\gamma < p_E. \tag{63}$$

We summarize all parameters required for the optimizations in Table 1 following the methodology in Sect. 3.

We increase the complexity through multiple optimizations to better understand the problem and the successive nonlinearities introduced. For this reason, we successively add stress constraints and filtering techniques to a pure thermoelectrical optimization with power constraints. Furthermore, we repeat this analysis for different material conditions for the model, from constant material properties at 350K, to nonlinear material properties with temperature, to the introduction of air material in the void regions and in between the thermocouple legs. The results from these successive optimizations are represented in Fig. 2 with an increased number of constraints and filtering techniques towards the right and increased model and material complexity further down. Each plot in this figure represents the density field for the 150th iteration or convergence conditions for each optimization with a linear colour scale with white representing void material and black full-density material.

Table 1 MMA optimization parameter summary according to Eqs. (25), (18), and (24) for the optimization results in Fig. 2

Parameter	Value	Parameter	Value
$V_{\min}$	0.01V	c_m	20,000
$V_{\max}$	0.06V	d_r	0.11 mm
p_E	5	P_{obj}	15 mW/mm
p_S	1	σ_0	10E6
p_σ	3	T_{ref}	298.15K
p_k	3	T_h	350K
q_{in}	$7500\ \mathrm{W/m^2}$	$\varepsilon_{\mathrm{KKT}}$	10^{-8}
β	64	$x_S^{(i=0)}$	0.5
μ	0.4	i_m	150

The pure thermoelectrical TO with power constraints but without stress or volume constraints is shown in Fig. 2a, e, and i. These plots show an asymmetry between each pellet, given their different thermoelectrical properties of p+ and n-type semiconductors. Notice that the Peltier effect is based on the change of energy of the electrons moving between different outer valence energy levels between two dissimilar semiconductors. Therefore, the effect only requires contact between dissimilar semiconductors. The optimization objective tries to reach an optimal configuration between decreasing the thermal conductivity and increasing the electrical conductivity of each semiconductor. Given the material properties used, see Appendix C, we use the same thermal conductivity for both semiconductors, and the optimization should leave the largest amount of the material with the lowest electrical conductivity at each operational temperature to compensate for it. Indeed, we observe that the electrical conductivity provided in Appendix C decreases with temperature; with the highest temperature located at the bottom surface of the thermocouple, the heat sink, the optimized pellets present the largest amount of material at this location, with the lowest amount of material at the cold top surface contact with the higher electrical conductivity. The optimizer also tries to reduce Joule heating concentrations by creating multiple electrical paths, avoiding hot spots and distributing the Peltier effect through multiple contacts along the cold surface.

A second set of optimizations include a stress constraint to 10 MPa (Fig. 2b, f and j). These optimizations maintain features of the pure thermoelectrical TO such as continuous paths for the electrical and thermal flow but also present joints and smaller contacts to the top and bottom surfaces to reduce the thermally induced stresses in the thermocouple. These joints are made through features of a single element and porous material. This is an undesirable and difficult-to-manufacture topology. A Helmholtz filter can introduce a length scale, removing all single-element features and providing mesh independence to the results. A third set of optimizations using a filter radius $d_r = 0.11$mm is shown in Fig. 2c, g, and k. A larger feature size increases the overall stresses in the structure, and the use of the same mechanical properties under an active stress constraint for both semiconductors leads to an increased symmetry between both legs. However, these results maintain intermediate density elements between the solid and void material. These intermediate densities can introduce thermoelectric artefacts due

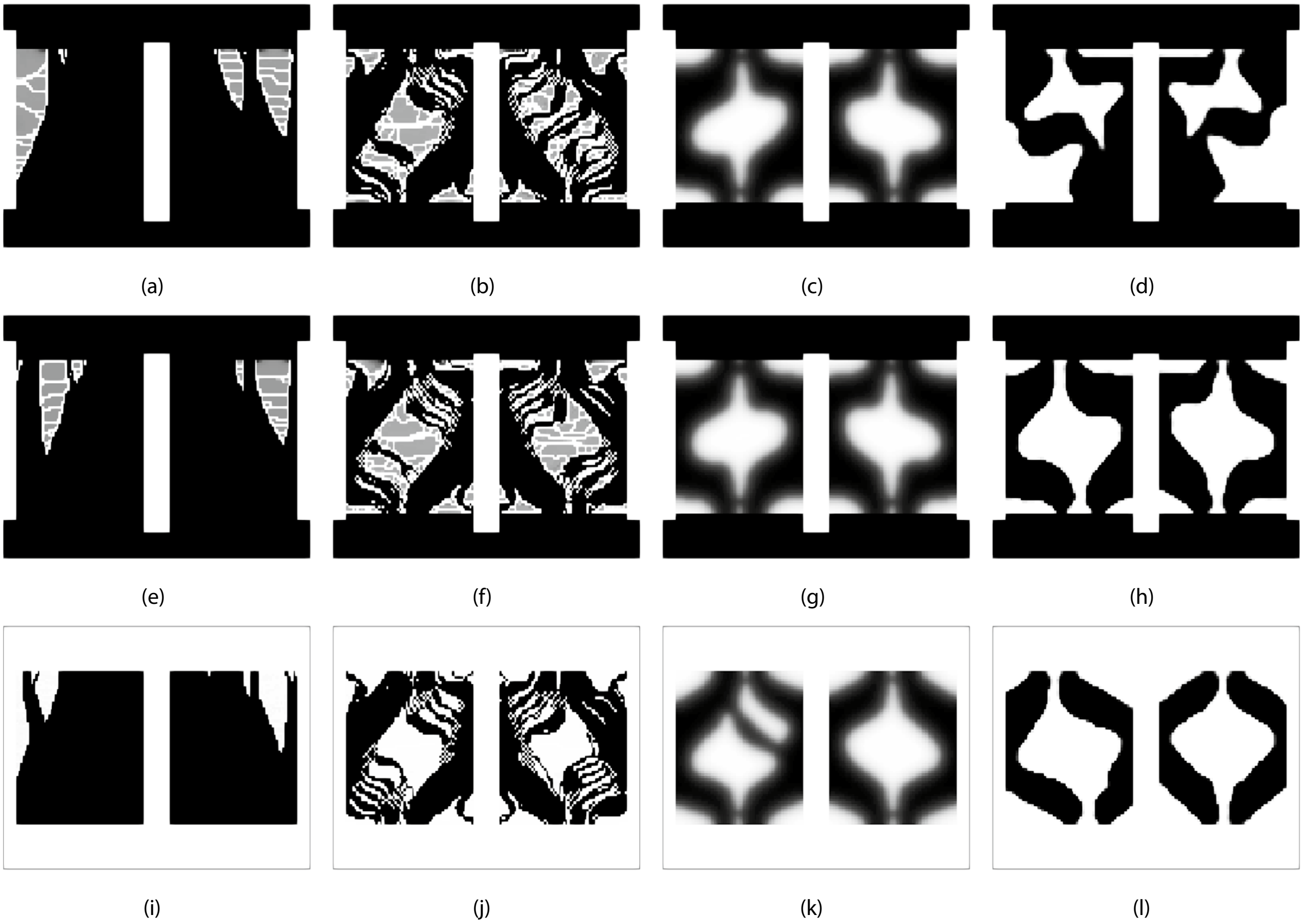

Fig. 2 Physical density field for 2D thermocouple optimizations, ranging from full-density elements (in black) to full-void elements (white). Grey elements represent regions with intermediate density values. Subfigures Fig. 2a to d use constant material properties at 350K. Subfigures Fig. 2e to h apply nonlinear properties with temperature. The nonlinear material properties and their values at 350K are described in Appendix C. Subfigures Fig. 2i to l also include air as a material in voids and between pellets. Fig. 2a, e, and i shows results from pure thermoelectric optimizations under power constraints, without filtering or stress constraints. Figure 2b, f and j includes stress and power constraints without filtering. Figure 2c, g, and k applies a Helmholtz filter in addition to stress and power constraints. Figure 2d, h, and l combines stress and power constraints with both Helmholtz and Heaviside filters. The values for each constraint and filtering technique are summarized in Table 1

to changes in Seebeck coefficient, the Thompson's effect, and temperature gradients.

To remove these intermediate densities, we introduce a Heaviside projection after the Helmholtz filtering to obtain a sharper transition between the void and solid material in Fig. 2d, h, and l. We use a Heaviside projection with $\mu = 0.4$ and a $\beta = 64$. This optimization requires modifying the initial $\boldsymbol{x}_\rho = 0.4$ and default parameters of MMA to obtain convergence and avoid a thermoelectric disconnection of the design. We reduce the movement of the asymptotes in MMA using a move limit, adjusting the increase and decrease rates of the asymptotes, and setting an initial asymptote value of 2%. The results maintain previously found design characteristics, with a crisp transition between solid and void material. We can see that each electrical path develops a rotational joint to accommodate thermal deformation. Between each joint, the algorithm increases the material amount to compensate for the reduced electrical conductance at the joints with smaller cross-sections.

To justify the Heaviside filtering and the impact of grey regions in Helmholtz filtering, the optimal configuration in Fig. 2f to h was modified by retaining elements with $x_e > 0.85$. These elements were assigned full density, while others were set to $x_e = 1e-6$. Figure 3 compares the new black-and-white designs with the original optimal geometry as $\Delta\Xi = \Xi_{\mathrm{BW}} - \Xi_{\mathrm{opt}}$, where Ξ represents the respective objective or constraint. The black design is coloured based on its temperature difference from the optimal design and deformed according to the displacement field difference, scaled by 1000. In Fig. 3a, grey areas are electrically disconnected, resulting in minimal thermal variation, with a total deviation of 0.38°C in localized areas, specifically at

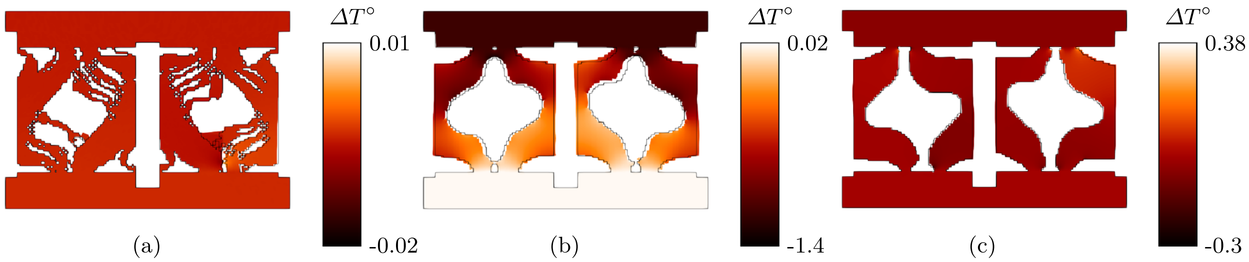

(a) (b) (c)

Fig. 3 Difference in the thermomechanical response between the black-and-white design (thresholded with $x_e > 0.85$ assigned full density and $x_e = 0.001$ otherwise) and the corresponding optimized design. The field differences are calculated for Fig. 2f to h in Fig. 3a to c, respectively. The coloured map illustrates the temperature field difference, computed as $\Delta\Xi_T = \Xi_{T,\mathrm{BW}} - \Xi_{T,\mathrm{opt}}$. The displacement field difference is shown as in the deformation of the geometry calculated as $\Delta\Xi_u = \Xi_{u,\mathrm{BW}} - \Xi_{u,\mathrm{opt}}$, scaled 1000 times for visualization, with respect to the original edges of the undeformed design

Table 2 Comparison between the optimized design results (shown in Fig. 2e to g) and the corresponding black-and-white design, obtained by thresholding elements with $x_p > 0.85$ to full material and the rest to void

	Fig. 3a	Fig. 3b	Fig. 3c
$\boldsymbol{\Phi}$	333.484419	334.142404	333.239808
C_p	5.9×10^{-5}	-8.3961×10^{-2}	-2.072×10^{-3}
C_σ	1.0×10^{-6}	2.10919×10^{-1}	1.9486×10^{-2}
$\Delta\boldsymbol{\Phi}$	-1.129×10^{-3}	-1.153401	-4.6457×10^{-2}
ΔC_p	5.9×10^{-5}	-8.3961×10^{-2}	-1.974×10^{-3}
ΔC_σ	4.0×10^{-6}	2.1092×10^{-1}	2.003×10^{-2}

The values for $\boldsymbol{\Phi}$, C_p, and C_σ correspond to the black-and-white design, and the differences are computed as $\Delta\Xi = \Xi_{\mathrm{BW}} - \Xi_{\mathrm{opt}}$, where Ξ denotes any of the considered objective or constraints, with subscripts BW and opt indicating the black-and-white design and the optimized design, respectively

Table 3 Comparison between the results obtained using constant material properties defined at 350K and those obtained from the same optimal designs using nonlinear material optimization (Fig. 2e to h)

	Fig. 2a	Fig. 2b	Fig. 2c	Fig. 2d
$\boldsymbol{\Phi}$	335.53	333.10	334.91	332.81
C_p	4.14×10^{-2}	4.69×10^{-2}	3.99×10^{-2}	4.57×10^{-2}
C_σ	–	-3.72×10^{-3}	-3.10×10^{-3}	-4.98×10^{-3}
$\Delta\boldsymbol{\Phi}$	-2.40×10^{-1}	-3.93×10^{-1}	-3.61×10^{-1}	-4.59×10^{-1}
ΔC_p	4.14×10^{-2}	4.69×10^{-2}	3.99×10^{-2}	4.58×10^{-2}
ΔC_σ	–	-1.04×10^{-2}	-9.49×10^{-3}	-1.17×10^{-2}

The values of $\boldsymbol{\Phi}$, C_p, and C_σ correspond to the results obtained using constant material properties, while the differences are computed as $\Delta\Xi = \Xi_{\mathrm{nonlin}} - \Xi_{\mathrm{cte}}$, where $\Xi \in \{\boldsymbol{\Phi}, C_p, C_\sigma\}$

the smallest electrical path contact with the cold surface. In contrast, Fig. 3b shows larger temperature changes up to 1.4°, particularly near the device centre along z. Figure 3c improves on the behaviour of Fig. 3b, with temperature differences of 0.38 in localized areas compared to the optimal design, without single-element joints. Table 2 presents the final values of the objectives and constraints for each black-and-white design, along with the differences from the optimal designs. The grey areas in Fig. 3a have minimal impact on the metrics compared to the filtered designs. The filtered designs show similar corrected objectives, differing only in the second decimal for the black-and-white designs. However, the objective difference from the optimized designs is two orders of magnitude larger in the design that uses only the Helmholtz filter. Finally, the stress constraint is not satisfied in all black-and-white designs, with the largest difference found in the design with only the Helmholtz filter.

Although the material properties are nonlinear, the study focuses on the range from 333 to 350K, where nonlinear effects are moderate compared to the full temperature range, as shown in Appendix C. This suggests that approximating the material properties at a fixed temperature may yield a sufficiently accurate geometry without requiring full nonlinear modelling. Therefore, optimization is performed using properties evaluated at 350K, as shown in Fig. 2a to d. The resulting density fields are then reevaluated using nonlinear material properties and the same voltage gradient. Table 3 presents the results, comparing the constant-property-based optimal design to the nonlinear case using $\Delta\Xi = \Xi_{\mathrm{nonlin}} - \Xi_{\mathrm{cte}}$. These results show lower objective and stress values but fail to meet the power constraint. The power deviation corresponds to a maximum increase of 0.7mW per thermocouple in the design shown in Fig. 2d. In this case, grey elements in Fig. 2c appear to limit both the increase in power and the reduction in stress. Nonlinear evaluation leads to temperatures up to 0.46° lower than those from constant-property models.

To account for conduction losses, an air model is introduced between the thermoelectric legs. This model uses a void thermal conductivity κ_v of 0.033 K/W and assigns the minimum value for the Young's modulus, electrical conductivity, and the Seebeck coefficient. The resulting density fields are shown in Fig. 2i to l. These fields resemble

Table 4 Comparison of optimal results considering two modelling approaches for void regions: treated as true void and as air

	Fig. 2i	Fig. 2j	Fig. 2k	Fig. 2l
Φ	336.41	334.20	336.14	334.06
$\Delta\Phi$	0.24	0.71	0.84	0.77

The values of Φ correspond to the results where void is modelled as air (shown in Fig. 2i to l), while the differences are computed as $\Delta\Xi = \Xi_{\text{air}} - \Xi_{\text{void}}$

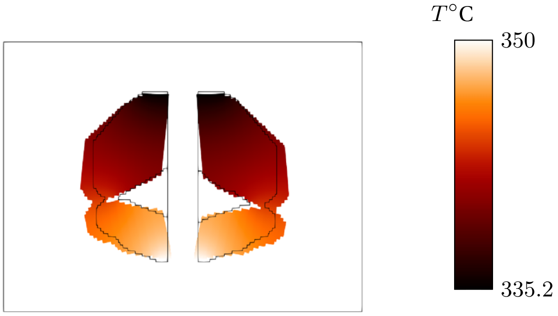

Fig. 4 Thermomechanical response of the optimal thermo-electro-mechanical design after 150 iterations with the power and stress constraints defined in Table 1 and a volume constraint of 50%. The figure shows all elements with $x_\rho > 0.1$, the mechanical deformation is shown in a coloured map that represents the temperature range. The displacements are introduced with a scale of 90 times their nominal value

previous designs but show greater separation between solid regions near the cold and hot surfaces due to the increased thermal resistance through the air. Grey regions vanish in these designs, as higher densities in those areas would worsen performance due to non-negligible thermal conductivity. Table 4 summarizes the objectives and constraints, comparing the air model designs to those with void materials Fig. 2e to h using $\Delta\Xi = \Xi_{\text{air}} - \Xi_{\text{void}}$. These optimizations show a temperature increase of up to 0.84° in the optimal geometries. The lowest difference arises in the pure thermoelectric optimization due to the larger optimal volume of semiconductors compared to stress-constrained optimizations. Air inclusion also raises stress levels, as the optimizer increases semiconductor material to counteract heat flux, expanding the contact area with mismatched α_T values. Compared to constant property assumptions, these losses have a more pronounced impact, making them significant for accurate optimization.

We perform one last optimization with all filters, considering air-conduction losses, and a volume constraint of 50%, close to 10% lower than the obtained volume for Fig. 2l optimization. We show the deformation field of the physical density field in Fig. 4 with a scale 90 times the actual deformation superposed to the undeformed edges. This figure shows the elements in the mesh with $x_\rho > 0.1$. The colour plot shows the temperature of this design for the maximum power allocation allowed of $P = 15\text{mW/mm}$. In these results, we can observe a contraction in the middle of the thermocouple and an expansion towards its outer edges, pivoting around the joint in each leg. The temperature field shows a similar profile to that of previous optimization, with losses in the order of 1.15°C.

The values of the objective function and all constraints for the first 150 MMA iterations for all optimizations are shown in Fig. 5. This figure includes the values for the objective aggregated temperature $\Psi(\mathbf{T}_{\boldsymbol{\Phi}})$ (Fig. 5a), the power consumption (Fig. 5b), the stress aggregated value $\Psi(\boldsymbol{\sigma}_{VM})$ (Fig. 5c), the voltage gradient across the thermocouple (Fig. 5d), and percentage of the original semiconductor volume (Fig. 5e). The objective for the filtered and volume constraint optimization, Fig. 4, is the one with highest moving rate by the end of the 150 iterations. Even for this case, the change in the objective is lower than a 0.2% between the last ten iterations. The delay in convergence for the Heaviside-filtered designs arises from the slow-moving limits imposed on the MMA optimizer. The temperature objective remains stable after 50 iterations for the rest of optimizations. There is also an initial jump in temperature caused by the excessive power consumption of the initial designs and by its subsequent lowering by MMA. The power constraint is satisfied for all optimizations and equal to the maximum available. The oscillation present for its value can also be correlated to the stress constraint. In the unfiltered and Helmholtz-filtered designs, there is a peak in the stress constraint that induces a lower voltage and power consumption, reducing the current and joule heating along the device and thermal deformations to satisfy it. These peaks are not present when we reduce the moving limits for MMA or in pure thermoelectrical optimization. While the stress constraint increases the complexity of the problem, it is active for all final results. It can reduce the stresses compared to the pure thermoelectrical optimization to a fifth of its initial value without compromising the temperature achieved.

We can observe the complexity of the design space field from the multiple designs obtained in Fig. 2, which can provide similar temperature profiles according to Fig. 5a. This can partly be achieved through the different final x_S shown in Fig. 5d. This plot shows that no design shares the same voltage gradient for the optimized temperature profile. Furthermore, the fact that the temperature obtained for the pure thermoelectrical optimization is higher than for the rest of the optimizations, with a difference of ≈ 2.5°C implies that there are multiple local optima and the stress constraint steers the optimizer towards new optima not reachable by MMA with the imposed parameters from the initial optimization. Furthermore, while the stress-constrained optimization provides one of the lowest temperature profiles and the Helmholtz filter decreases these gains due to the introduced

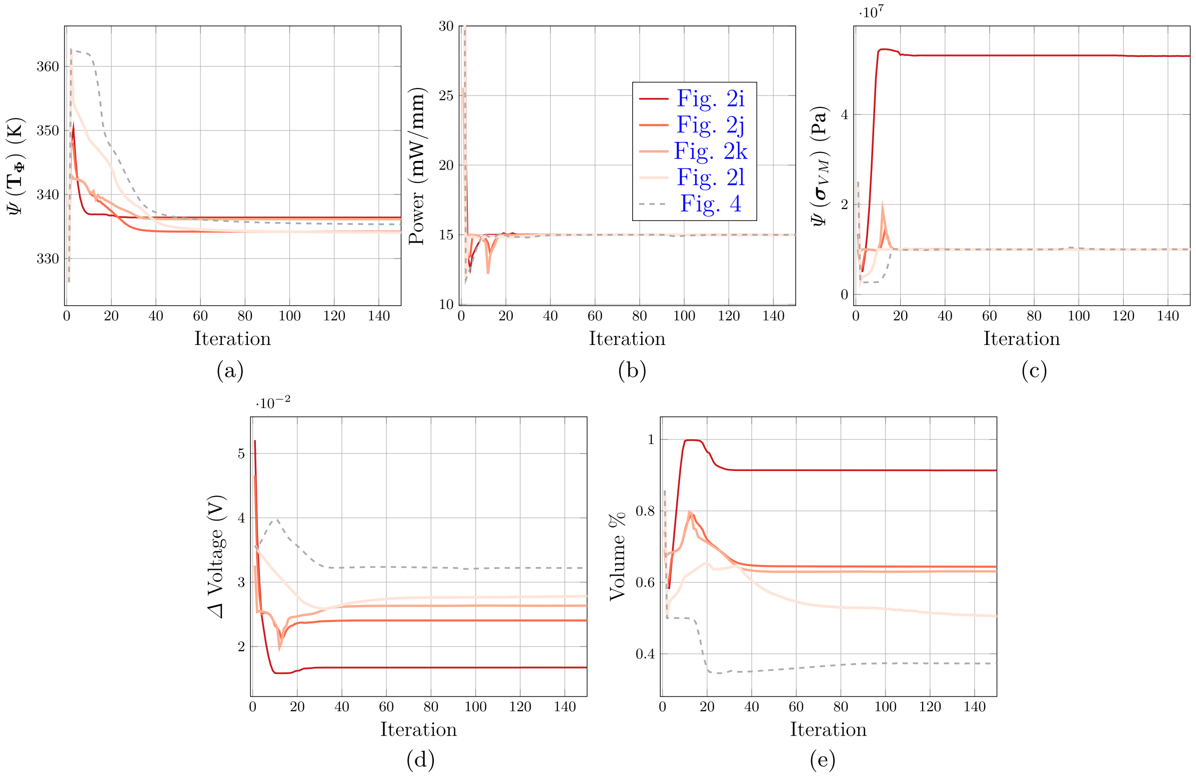

Fig. 5 Convergence results for the 2D TO for the 4 different cases summarized in Fig. 2. Each plot shows the evolution of a different variable, including Fig. 5a the objective temperature; Fig. 5b power; Fig. 5c stress; Fig. 5d voltage gradient; and Fig. 5e volume constraints

intermediate densities, the Heaviside filter can recover these results with a more manufacturable design.

The higher sensitivity to the voltage design variable compared to the density design variables can be seen as the overall volume of the design keeps changing. Still, the impact on the objective temperature is lower than 1% of its value. In particular, for the volume-unconstrained and unfiltered models, there is an increase in the volume of disconnected areas in the latter iterations of the optimizer. Furthermore, the convergence to lower design volumes without volume constraints due to the search for low thermal conductivity reduces the semiconductor material we need to use in these designs. We can see that while we converge to lower volumes for stress-constrained optimisations, this does not lead to worse objective performance. In all cases, the lower volume is compensated by a higher voltage gradient across the thermocouple, leading to multiple local minima present, dependent on this design variable. The intermediate densities are also considered adverse for the objective as the design obtained by only using the Helmholtz filter increases its value compared to the other stress-constrained designs. Regarding convergence, we present the first 100 MMA iterations, which are sufficient to ensure convergence for all objective functions. However, in the case of the Heaviside-filtered optimizations, the lower bounds for the MMA parameters lead to larger movements of the density design variables when we reach the maximum iteration value.

4.2 3D results

The 3D model dimensions are the same as those of the 2D model. However, we extend the design space outside the contact area. The parameters of the model's yz plane are shown in Fig. 6. The square cross-section across z is of 0.5 mm with a symmetry condition is at $z = 0$. Given this symmetry condition, we use a power constraint of 7.5mW. $l_1 = 0.2$mm and $l_2 = 0.05$mm delineate the extra design space along the third dimension. Each semiconductor leg is meshed with a $24 \times 24 \times 13$ and regular grid, with a total of 7488 serendipity 20-node elements (H20) per leg.

We perform two 3D optimizations without air modelling between pellets to reduce DOFs, including a thermal conductivity of $\kappa_v = 0.033 WK/m$. Each optimization is run with either no volume constraint or 40% volume constraint. Both optimizations use Helmholtz and Heaviside filters. The same power and stress constraints, filtering, density, and voltage design variables and limits, and MMA parameters as in the 2D optimizations are applied, as summarized in Table 1. The filtering parameters are $\mu = 0.4$, $\beta = 64$, an initial semiconductor density of 0.4, and MMA moving limits of 2%.

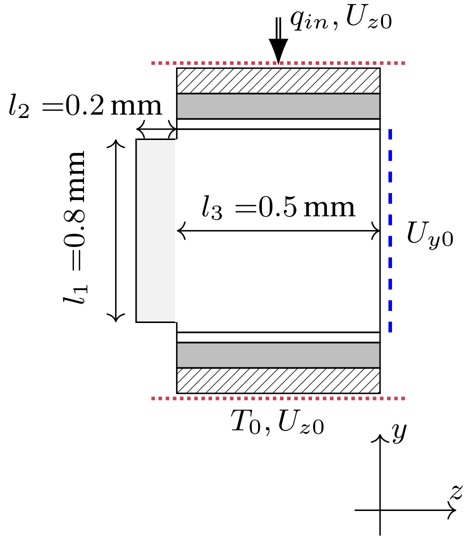

Fig. 6 3D thermocouple FEM model modifications to Fig. 1. The figure shows the lateral view of Fig. 1 for a 3D TO model with an increase in material along the z direction and a symmetry boundary condition for the mechanical DOFs

We show the physical density design variables with values $\mathbf{x}_\rho > 0.1$ for an optimization of the 3D geometry following the values in Table 1, using the Helmholtz and Heaviside filter in Fig. 7, and the MMA parameters are those used for the results in Fig. 2h. This plot includes the non-semiconductor materials as a transparent volume and the semiconductor material as a colour plot representing its temperature. The two results represent an optimized design with no volume constraint in Fig. 7a and an optimized design with a volume constraint of 40% in Fig. 7b. These plots lead to a quasi-symmetrical design for both pellets. As with the 2D results, the mechanical stress constraint dominates the problem. The volume-constrained model leads to a *tuning fork* or U-shaped geometry featuring a central contact line along x on the heat sink surface aligned with the middle of the z axis. This central contact then branches into two separate contacts located at the edges in z of the heat injection surface. The unconstrained volume optimization leads to a structure with larger changes along the x axis and a rhomboid hole in the yz plane cross-section turning around the y axis. In both cases, the resulting topology accommodates the deformations with a topology focussed on the yz cross-section.

The convergence history is plotted in Fig. 8 for the temperature and volume. The volume-constrained optimization has found a 35% original volume design compared to the original design with temperature objectives with less than 0.1° difference with a voltage up to 4 times higher than in the volume-unconstrained optimization. This indicates the presence of non-convex local minima dependent on the voltage that can be reached through the volume constraint. We can further compare the 2D and 3D results by extruding the 2D design into the third dimension (i.e. 2.5D) to the equivalent 3D dimension. The equivalent final volumes of the optimal designs in the 3D configuration are lower than in the 2.5D case. The 3D model also provides a lower optimal temperature of 326K compared to the 334K obtained by the 2.5D design given its larger design space freedom.

5 Summary and conclusions

This paper deals with the thermo-electro-mechanical optimization of thermocouples. We do so by linearizing and decoupling the mechanical and thermoelectric DOFs. This approach reduces the memory required to solve the thermo-electro-mechanical problem and is valid for problems with small thermal deformations. As a result, this approach can provide designs that minimize stress concentrations and increase their expected lifetime for thermoelectrical devices.

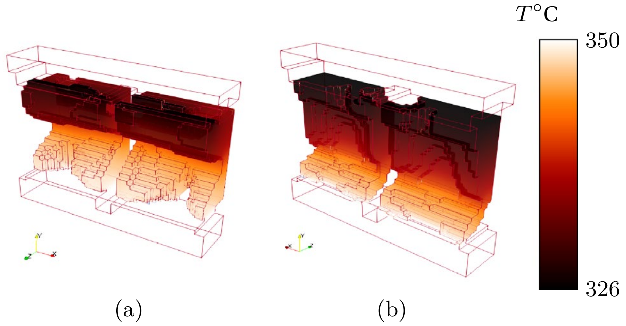

(a) (b)

Fig. 7 Results of a 3D TO of a thermocouple with stress constraints using no volume constraint Fig. 7a or a volume constraint of 40% the original volume Fig. 7b. We plot the topology results either for convergence conditions or the 150th iteration. The figure shows the resulting elements with more than 10% density in the design domain and the axis system for each figure. The colour plot shows the temperature gradient of the semiconductor material

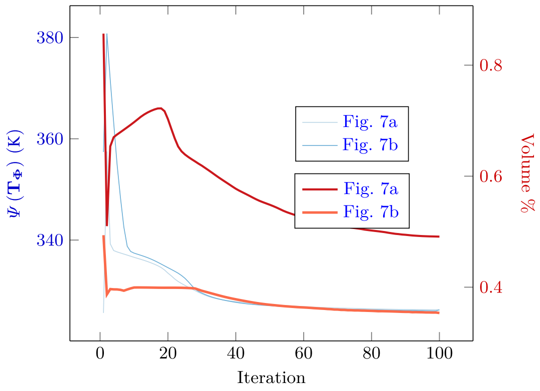

Fig. 8 Temperature objective in blue and volume percentage in reds for both results in Fig. 7 along each iteration of the optimizer

In the model proposed, we consider a single pellet, and the resulting TEC could be built, making all pellets follow it. However, in reality, some effects are not taken into account when we model the entire device. In particular, the edges and inner regions of the TEC will not absorb the same amounts of heat. This could be considered through homogenization techniques, where each thermocouple can be a unit cell of the final design. The optimization could also incorporate the orientation, location, and number of thermocouples. However, the use of homogenization may increase the number of FEM solves. Neglecting Joule heating in the device can convert the nonlinear thermoelectric equations into a linear system without needing a Newton–Raphson solver for temperature-constant material properties (Fragoso et al. 2005). If these simplifications are taken, the optima found must be post-processed to verify their accuracy compared to the nonlinear models. Future studies could also be conducted on the effect of the overall dimensions of the initial thermocouple design and surrounding materials to optimize the design further. These further studies should also involve integrating boundary-dependent radiation loads into the optimization procedure as radiation is shown by Bjørk et al. (2014) to have a significant contribution to thermoelectric devices efficiency the larger the internal spacing between thermoelectric legs. Onodera and Yamada (2025) already show a methodology to integrate these loads in thermomechanical level-set TO problems, and a simple boundary identification algorithm could also be adapted to environment radiation loading (Ibhadode et al. 2020).

Even with our simplifying assumptions, the optimizations led to multiple optima with similar objective values and different geometries. This seems to be related to the use of the voltage as a design variable, allowing further flexibility in the design space. However, this flexibility over the electric working point can flatten the design space, hindering convergence. Although the volume constraint can steer the algorithm towards a new solution, this is not ideal as we do not know the optimal volume for a given working point. Techniques for exploring the overall design space, such as genetic algorithms, could be helpful in understanding the location of these multiple minimum values. Deflation, relaxation, or preconditioning techniques could be used to find other minima (Farrell et al. 2015). Furthermore, the effect of penalization coefficients on the material properties and their relative ranges has already been shown to affect the overall non-convexity and the convergence of the problem objective and constraints. In the past, heuristic algorithms have been used to study the effects of optimization parameters, (Ait Ouchaoui et al. 2023). However, heuristics are computationally expensive and must be applied to each problem studied separately. While analytical models help understand the physics behind the problem, techniques to evaluate the fitness of an objective or constraint in higher dimensionality should be explored. New high-dimensionality projection techniques could be used for this purpose, allowing the selection between different initial parameter values (Espadoto et al. 2023).

We also see the need for a length scale filter to avoid single-element features in thermo-electro-mechanical optimizations and to decouple the solution from the mesh resolution in the problem involving material nonlinearities. We find that the Helmholtz filter can introduce this length scale. Still, a Heaviside filtering is also needed to provide a sharp design and avoid the intermediate densities from the Helmholtz filter that provides worse optimized objective values. Convergence to lower objectives is also achieved without the need to reinitialize the optimization to gradually increase the filter sharpness. We find that a $\mu \geq 64$ is enough provide a black-and-white design with minimal grey regions in the thermo-electro-mechanical optimization problem. Zhou et al. (2015) provide an alternative approach to introduce a length scale function based on constraints on the filtered fields that could also improve the problem solution without introduction of grey regions. We notice as well the tendency of the pure thermoelectrical TO with air losses to remove grey elements, which itself could act as a filter to provide sharp edges geometries with the cost of a single thermoelectrical calculation per MMA iteration for different problems. Different constraints could also be implemented to prevent small features. In particular, the current flow seems attractive for this purpose. Smaller feature sizes lead to higher electrical resistance; avoiding small current flows in our full-density design could remove these features. Furthermore, the imposed constraints do not limit the possibility of dangerous or fatal situations during dynamic situations regarding current flow concentrations or thermal shocks, which should be considered.

The use of stress constraints, while reducing stresses within the assembly that elongate the device's lifespan, further increases the complexity of the problem. Note that we use no contact formulation, and the small size of these devices and the more flexible designs can lead to short circuits that must be avoided. This could be considered a displacement constraint in our optimization or the addition of material between the legs in our model. To simplify the problem formulation further, we could also consider only the most critical solder regions as defined in Awrejcewicz et al. (2020). Another further simplification could be reducing the design space of the mechanical constraints to a single pellet, given the dominance of the stress constraint over the thermoelectric variables. This would require special mesh preconditioning between both pellets and mirroring the sensitivities to each pellet.

In summary, we propose a TO approach that uses stress constraints in thermoelectrical problems for cooling applications. Although the proposed formulation can lower

Table 5 Matrix and vector sizes in thermo-electro-mechanical FEM (Quad8/Hex20)

Symbol	Description	2D (Q8)	3D (H20)
j	Curr. density	2×1	3×1
q	Heat flux	2×1	3×1
$\hat{\sigma}$	Stress (Voigt)	3×1	6×1
u	Displacement	16×1	60×1
t	Temperature	8×1	20×1
v	Elec. potential	8×1	20×1
C_0	Elastic matrix	3×3	6×6
β_T	Thermal stress	3×1	6×1
e_{tr}	Trace operator vector	3×1	6×1
$\boldsymbol{\nabla} N$	Shape func. (scalar)	8×3	20×3
N	Shape func. (scalar)	8×1	20×1
N_U	Shape func. (disp)	16×1	60×1
B	Strain-displ. mat	3×16	6×60
r_u	Mech. residual	16×1	60×1
r_t	Thermal residual	8×1	20×1
r_v	Elec. residual	8×1	20×1

stress concentration measurements—up to 5 times lower compared to regular thermoelectrical optimization in the proposed examples—the non-convexity problem still leads to challenges in finding local minima. Furthermore, manufacturing the optimized thermocouples should still be studied and further implemented in the optimization process.

Residual derivatives

In this appendix, we develop the required derivatives of the residual for the thermo-electro-mechanical FEM system for the calculation related to of the adjoint sensitivities and tangent matrix.

To derive the residual derivatives for the thermo-electro-mechanical finite element system, the element level dimensions of the involved matrices and vectors must be established. These sizes vary with the element type and determine the structure of both the tangent matrix and the adjoint sensitivities. Table 5 presents the relevant quantities at the element level for quadratic 2D (Quad8) and 3D (Hex20) elements, including field variables, constitutive matrices, and shape function representations. This information defines the computational framework used in the derivation of the sensitivity equations.

The first derivatives we need to define are the derivatives of the residual with respect to the element level state vector $\mathbf{s}$ composed of the element level displacement $\mathbf{u}$, temperature $\mathbf{t}$, and voltage $\mathbf{v}$ degrees of freedom. These derivatives are

$$\begin{aligned}\frac{\partial \mathbf{r_u}}{\partial \mathbf{t}} &= \mathbf{k}_\Theta + \int_\Omega \mathbf{B}^\intercal \frac{\partial \boldsymbol{\beta}_T}{\partial T} \theta \mathbf{N}^\intercal \, \mathbf{d}\Omega \\ &\quad - \int_\Omega \mathbf{B}^\intercal \frac{\partial \mathbf{C}}{\partial T} \mathbf{B}\mathbf{u}\mathbf{N}^\intercal \, \mathbf{d}\Omega \,,\end{aligned} \tag{64}$$

$$\frac{\partial \mathbf{r_u}}{\partial \mathbf{u}} = -\mathbf{k}_\mathbf{U} \,, \tag{65}$$

$$\frac{\partial \mathbf{r_t}}{\partial \mathbf{t}} = - \int_\Omega \boldsymbol{\nabla}\mathbf{N} \frac{\partial \mathbf{q}}{\partial \mathbf{t}} \, \mathbf{d}\Omega + \int_\Omega \mathbf{N} (\frac{\partial \mathbf{j}}{\partial \mathbf{t}}^\intercal \boldsymbol{\nabla}\mathbf{N}^\intercal \mathbf{v})^\intercal \, \mathbf{d}\Omega \,, \tag{66}$$

$$\begin{aligned}\frac{\partial \mathbf{r_t}}{\partial \mathbf{v}} &= - \int_\Omega \boldsymbol{\nabla}\mathbf{N} \frac{\partial \mathbf{q}}{\partial \mathbf{v}} \, \mathbf{d}\Omega \\ &\quad + \int_\Omega \mathbf{N} (\frac{\partial \mathbf{j}}{\partial \mathbf{v}}^\intercal \boldsymbol{\nabla}\mathbf{N}^\intercal \mathbf{v})^\intercal \, \mathbf{d}\Omega \\ &\quad + \int_\Omega \mathbf{N}\mathbf{j}^\intercal \boldsymbol{\nabla}\mathbf{N}^\intercal \, \mathbf{d}\Omega \,,\end{aligned} \tag{67}$$

$$\frac{\partial \mathbf{r_v}}{\partial \mathbf{t}} = - \int_\Omega \boldsymbol{\nabla}\mathbf{N} \frac{\partial \mathbf{j}}{\partial \mathbf{t}} \, \mathbf{d}\Omega \,, \tag{68}$$

$$\frac{\partial \mathbf{r_v}}{\partial \mathbf{v}} = - \int_\Omega \boldsymbol{\nabla}\mathbf{N} \frac{\partial \mathbf{j}}{\partial \mathbf{v}} \, \mathbf{d}\Omega \,. \tag{69}$$

The temperature derivatives of $\mathbf{C}$ and β_T are

$$\begin{aligned}\frac{\partial \mathbf{C}}{\partial T} &= \mathbf{C}_0 \bar{x}_\rho^{p_E} \frac{\partial E}{\partial T}, \\ \frac{\partial \boldsymbol{\beta_T}}{\partial T} &= \frac{\bar{x}_\rho^{p_E}}{1 - 2\nu} \mathbf{e}_{\mathrm{tr}} \left(\alpha_T \frac{\partial E}{\partial T} + E \frac{\partial \alpha_T}{\partial T} \right).\end{aligned} \tag{70}$$

From these equations, we can recognize that the derivatives of the thermoelectrical degrees of freedom concerning the displacements are zero,

$$\frac{\partial \mathbf{r_t}}{\partial \mathbf{u}} = \mathbf{0}, \qquad \frac{\partial \mathbf{r_v}}{\partial \mathbf{u}} = \mathbf{0}, \qquad \frac{\partial \mathbf{r_u}}{\partial \mathbf{v}} = \mathbf{0}. \tag{71}$$

These equations still require the calculation of the derivative of the heat and current flows with respect to the nodal degrees of freedom,

$$\begin{aligned}\frac{\boldsymbol{\partial} \mathbf{j}}{\boldsymbol{\partial} \mathbf{v}} &= - \gamma \boldsymbol{\nabla}\mathbf{N}^\intercal, \\ \frac{\boldsymbol{\partial} \mathbf{j}}{\boldsymbol{\partial} \mathbf{t}} &= - \alpha\gamma \boldsymbol{\nabla}\mathbf{N}^\intercal - \frac{\partial \alpha}{\partial T} \gamma \boldsymbol{\nabla}\mathbf{N}^\intercal \mathbf{t}\mathbf{N}^\intercal - \frac{\partial \gamma}{\partial T} \alpha \boldsymbol{\nabla}\mathbf{N}^\intercal \mathbf{t}\mathbf{N}^\intercal, \\ \frac{\boldsymbol{\partial} \mathbf{q}}{\boldsymbol{\partial} \mathbf{v}} &= \alpha(\mathbf{N}^\intercal \mathbf{t}) \frac{\partial \mathbf{j}}{\partial \mathbf{v}}, \\ \frac{\boldsymbol{\partial} \mathbf{q}}{\boldsymbol{\partial} \mathbf{t}} &= \alpha(\mathbf{N}^\intercal \mathbf{t}) \frac{\partial \mathbf{j}}{\partial \mathbf{v}} + \frac{\partial \alpha}{\partial T} \left(\mathbf{N}^\intercal \mathbf{t}\right) \mathbf{j} + \alpha \mathbf{j}\mathbf{N}^\intercal + \frac{\partial \alpha}{\partial T} \mathbf{j}\mathbf{N}^\intercal \mathbf{t}\mathbf{N}^\intercal \\ &\quad - \kappa \boldsymbol{\nabla}\mathbf{N}^\intercal - \frac{\partial \kappa}{\partial T} \boldsymbol{\nabla}\mathbf{N}^\intercal \, \mathbf{t}\mathbf{N}^\intercal.\end{aligned} \tag{72}$$

The derivative and formulation of the thermoelectrical material properties with respect to the temperature are shown in Appendix C, completing these sensitivities.

We also require the sensitivities of the residual with respect to its physical density design variable for the MMA algorithm. The sensitivities of the thermoelectrical element level residuals with respect to the physical design are

$$\begin{aligned}\frac{\partial \mathbf{r_t}}{\partial \bar{x}_\rho} &= -\int_\Omega \nabla\mathbf{N}\frac{\partial \mathbf{q}}{\partial \bar{x}_\rho}\,\mathbf{d}\Omega + \int_\Omega \mathbf{N}(\frac{\partial \mathbf{j}}{\partial \bar{x}_\rho}^{\intercal}\nabla\mathbf{N}^{\intercal}\mathbf{v})^{\intercal}\,\mathbf{d}\Omega,\\ \frac{\partial \mathbf{r_v}}{\partial \bar{x}_\rho} &= -\int_\Omega \nabla\mathbf{N}\frac{\partial \mathbf{j}}{\partial \bar{x}_\rho}\,\mathbf{d}\Omega.\end{aligned} \tag{73}$$

Knowing that the heat and current flow derivatives, with material properties dependent only on each elemental density variable,

$$\begin{aligned}\frac{\partial \mathbf{j}}{\partial \bar{x}_\rho} &= -\frac{\partial \gamma}{\partial \bar{x}_\rho}\left(\nabla\mathbf{N}^{\intercal}\mathbf{v} + \alpha\nabla\mathbf{N}^{\intercal}\mathbf{t}\right) - \gamma\frac{\partial \alpha}{\partial \bar{x}_\rho}\nabla\mathbf{N}^{\intercal}\,\mathbf{t},\\ \frac{\partial \mathbf{q}}{\partial \bar{x}_\rho} &= \frac{\partial \alpha}{\partial \bar{x}_\rho}\left(\mathbf{N}^{\intercal}\mathbf{t}\right)\mathbf{j} + \alpha\left(\mathbf{N}^{\intercal}\mathbf{t}\right)\frac{\partial \mathbf{j}}{\partial \bar{x}_\rho} - \frac{\partial \kappa}{\partial \bar{x}_\rho}\nabla\mathbf{N}^{\intercal}\mathbf{t}.\end{aligned} \tag{74}$$

Finally, the derivatives of the material properties with respect to their elemental, following Eq. (24), value are

$$\begin{aligned}\frac{\partial \alpha}{\partial \bar{x}_\rho} &= p_\alpha \bar{x}_\rho^{\,p_\alpha - 1}(\alpha_0 - \alpha_{\min}),\\ \frac{\partial \kappa}{\partial \bar{x}_\rho} &= p_\kappa \bar{x}_\rho^{\,p_\kappa - 1}(\kappa_0 - \kappa_{\min}),\\ \frac{\partial \gamma}{\partial \bar{x}_\rho} &= p_\gamma \bar{x}_\rho^{\,p_\gamma - 1}(\gamma_0 - \gamma_{\min}).\\ \frac{\partial E}{\partial \bar{x}_\rho} &= p_E \bar{x}_\rho^{\,p_E - 1}(E_0 - E_{\min}).\end{aligned} \tag{75}$$

where the last two components have been calculated in Eq. (73). Finally, the derivative of the displacement associated residual at element level is

$$\begin{aligned}\frac{\partial \mathbf{r_u}}{\partial \bar{x}_\rho} &= -\frac{\partial \mathbf{k}_U}{\partial \bar{x}_\rho}\mathbf{u} + \frac{\partial \mathbf{k}_\Theta}{\partial \bar{x}_\rho}\boldsymbol{\theta},\\ \frac{\partial \mathbf{k_U}}{\partial \bar{x}_\rho} &= \int_\Omega \mathbf{B}^{\intercal}\frac{\partial \mathbf{C}}{\partial \bar{x}_\rho}\mathbf{B}\,\mathbf{d}\Omega,\\ \frac{\partial \mathbf{k_\Theta}}{\partial \bar{x}_\rho} &= \int_\Omega \mathbf{B}^{\intercal}\frac{\partial \boldsymbol{\beta}_T}{\partial \bar{x}_\rho}\mathbf{N}^{\intercal}\,\mathbf{d}\Omega.\end{aligned} \tag{76}$$

Depending on the derivative of the constitutive equation and thermoelastic material properties

$$\begin{aligned}\frac{\partial \mathbf{C}}{\partial \bar{x}_\rho} &= \mathbf{C}_0 p_E \bar{x}_\rho^{p_E - 1}(E_0 - E_{\min}),\\ \frac{\partial \boldsymbol{\beta}_T}{\partial \bar{x}_\rho} &= \frac{\left(p_E \bar{x}_\rho^{p_E - 1}(E_0 - E_{\min})\right)}{1 - 2\nu}\mathbf{e}_{\mathrm{tr}}\alpha_T,\end{aligned} \tag{77}$$

The derivatives of each material property with respect to the temperature field are provided in Appendix C as Eq. (85) using the coefficients in Table 7.

Finite differences and sensitivity validation

To validate the sensitivities within our code, we use forward finite differences for a simplified problem to obtain and compare the sensitivity values.

Let the objective function or constraint be denoted by $f(x_i)$, where x_i is the design variable. The finite difference approximation of the sensitivity with respect to the design variable x_i is given by

$$\frac{\mathrm{d}f}{\mathrm{d}x_i}(\epsilon) \approx \frac{f(x_i + \epsilon) - f(x_i)}{\epsilon}, \tag{78}$$

where ϵ is a small perturbation. The error between the finite difference and the FEM formulation for the sensitivities in Sect. 3 can be quantified by the relative error between both

$$\delta_{\mathrm{rel}}(\epsilon) = \left|\frac{\frac{\mathrm{d}\psi}{\mathrm{d}x_i} - \frac{\mathrm{d}f}{\mathrm{d}x_i}(\epsilon)}{\frac{\mathrm{d}\psi}{\mathrm{d}x_i}}\right|. \tag{79}$$

Using the Taylor approximation for $f(x_i + \epsilon)$, we can also observe that the relative error scales with

$$\delta_{\mathrm{rel}}(\epsilon) \approx \frac{\epsilon}{2}\left|\frac{\frac{\mathrm{d}[}{\mathrm{d}2}]f x_i}{\frac{\mathrm{d}f}{\mathrm{d}x_i}}\right| + \mathcal{O}(\epsilon^2). \tag{80}$$

In a log–log plot of $\delta_{\mathrm{rel}}(\epsilon)$ versus ϵ, we can make a prediction of the expected shape of the convergence of finite differences, expressing this relationship as

$$\log\left(\delta_{\mathrm{rel}}(\epsilon)\right) \approx \log\left(\left|\frac{\frac{\mathrm{d}[}{\mathrm{d}2}]f x_i}{2\frac{\mathrm{d}f}{\mathrm{d}x_i}}\right|\right) + \log(\epsilon), \tag{81}$$

where the first variable is a constant, the slope of this plot is ≈ 1, indicating first-order convergence.

We now apply finite differences to the same model as for the optimization in Fig. 2f with a reduced mesh to 3 x 3 within each semiconductor and all possible design variable configurations (Fig. 9). To validate the sensitivity

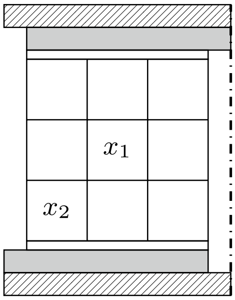

Fig. 9 Mesh simplification description for a coarse mesh from the model used in Sect. 4 and location of the studied design variables for the finite differences validation, x_1 and x_2, in one of the thermocouple legs

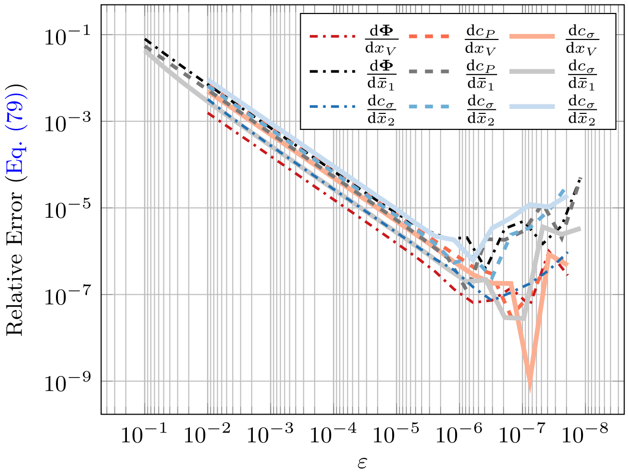

Fig. 10 Convergence of error with ε for each constraint and objective function used

results obtained via topology optimization, the error is plotted as a function of ϵ. The perturbation ϵ is varied, and the error is computed for each value. This comparison provides insight into the accuracy of the finite difference method relative to the FEM solution. This figure shows a linear rate of convergence for all objectives and constraints until the rounding errors dominate the problem for $\epsilon < 10^{-6}$ and errors under 10^{-5} at these perturbation levels. The volume constraint is removed from this validation as it can be validated through the volume calculation of the elements themselves (Fig. 10).

Material properties

There are multiple studies of the properties of thermoelectrical materials within the literature. We use the measured thermoelectric values for Bi_2Te_3 from Witting et al. (2019), where the effect of doping agents in Bi_2Te_3 over its material properties is studied. The thermal expansion values with respect to temperature for Bi_2Te_3 are taken from Pavlova et al. (2011). The experimental data have been fitted to a sixth-order polynomial,

$$f_p(T) = a_6T^6 + a_5T^5 + a_4T^4 + a_3T^3 + a_2T^2 + a_1T + a_0 \tag{82}$$

which allows the capture of the quadratic behaviour of the materials. For each material property, we fit this polynomial to the temperature ranges provided and to a constant value for higher or lower values to avoid discontinuities in the definition,

$$f(T) = \begin{cases} f_p(T_0) & \text{if } T < T_0, \\ f_p(T) & \text{if } T_0 \leq T \leq T_1 \\ f_p(T_1) & \text{if } T > T_1 \end{cases} \tag{83}$$

To have a continuous material model up to $\mathcal{C}^1$, we enforce a zero derivative in the intersection point of the functions, $f_p'(T_0) = f_p'(T_1) = 0$. Notice that for an accurate result, we must ensure the optimization lies within the measured temperature range.

The derivatives of these functions with respect to the temperature required to calculate the residual can be written as

$$f'(T) = \begin{cases} 0 & \text{if } T < T_0 \\ f_p'(T) & \text{if } T_0 \leq T \leq T_1 \\ 0 & \text{if } T > T_1 \end{cases} \tag{84}$$

where $f'(T)$ is

$$f_p'(T) = 6a_6T^5 + 5a_5T^4 + 4a_4T^3 + 3a_3T^2 + 2a_2T + a_1. \tag{85}$$

The temperature-dependent material properties used are plotted in Fig. 11 together with the experimental data as dots and the polynomial coefficients for each are provided in Table 6.

The other materials involved in a thermocouple are treated as temperature constants for simplicity purposes, and their properties are summarized in Table 7.

In all these materials, the Seebeck coefficient is considered to be zero, either due to the lack of electrical conductivity of the material or for a symmetrical material distribution in the models.

Note that E represents Young's modulus, ν represents Poisson's ratio, κ represents thermal conductivity, α represents the Seebeck coefficient, α_T represents the coefficient of thermal expansion, and σ is the electrical conductivity. The σ value of the ceramic AlN is not provided as there is no expected electrical current flow through the material. The mechanical properties of Bi_2Te_3 are also considered equal for the $p+$ and $n-$ semiconductors. In terms of the α, all materials are considered to have zero thermal stresses at 25.15°C.

Table 6 Coefficients for the 6th order polynomial fit for each semiconductor material according to Eq. (85)

Fit	a_0	a_1	a_2	a_3	a_4	a_5	a_6	T_0(K)	T_1(K)	$f_p(350K)$
κ	−76.4	1.23	−0.00764	2.45e−05	− 4.36e−08	4.09e−11	− 1.59e−14	235.48	605.34	2.717 W K/m
σ_p	− 2.73e7	5.88e5	− 4996	21.95	−0.053	6.70e−05	− 3.46e−08	173.46	451.56	1.839e05 S/m
σ_n	− 3.31e7	4.75e5	− 2768	8.48	−0.0144	1.29e−05	− 4.75e−09	289.17	618.62	1.787E05 S/m
α_p	0.00396	− 8.22e−05	7.00e−07	− 3.09e−09	7.47e−12	− 9.40e−15	4.80e−18	177.19	478.23	1.296e−04 V/K
α_n	−0.0253	0.000379	− 2.37e−06	7.81e−09	− 1.44e−11	1.42e−14	− 5.75e−18	292.82	529.42	-1.385E-04 V/K
α_T	2.841e−06	9.245e−08	− 2.341e−10	3.668e−13	− 9.482e−16	1.636e−18	− 9.464e−22	35	650	14.86e−6 1/K

The temperature range for the fit is represented in the last 2 columns as T_0 and T_1. The evaluated value at $T = 350$ K is shown in the last column

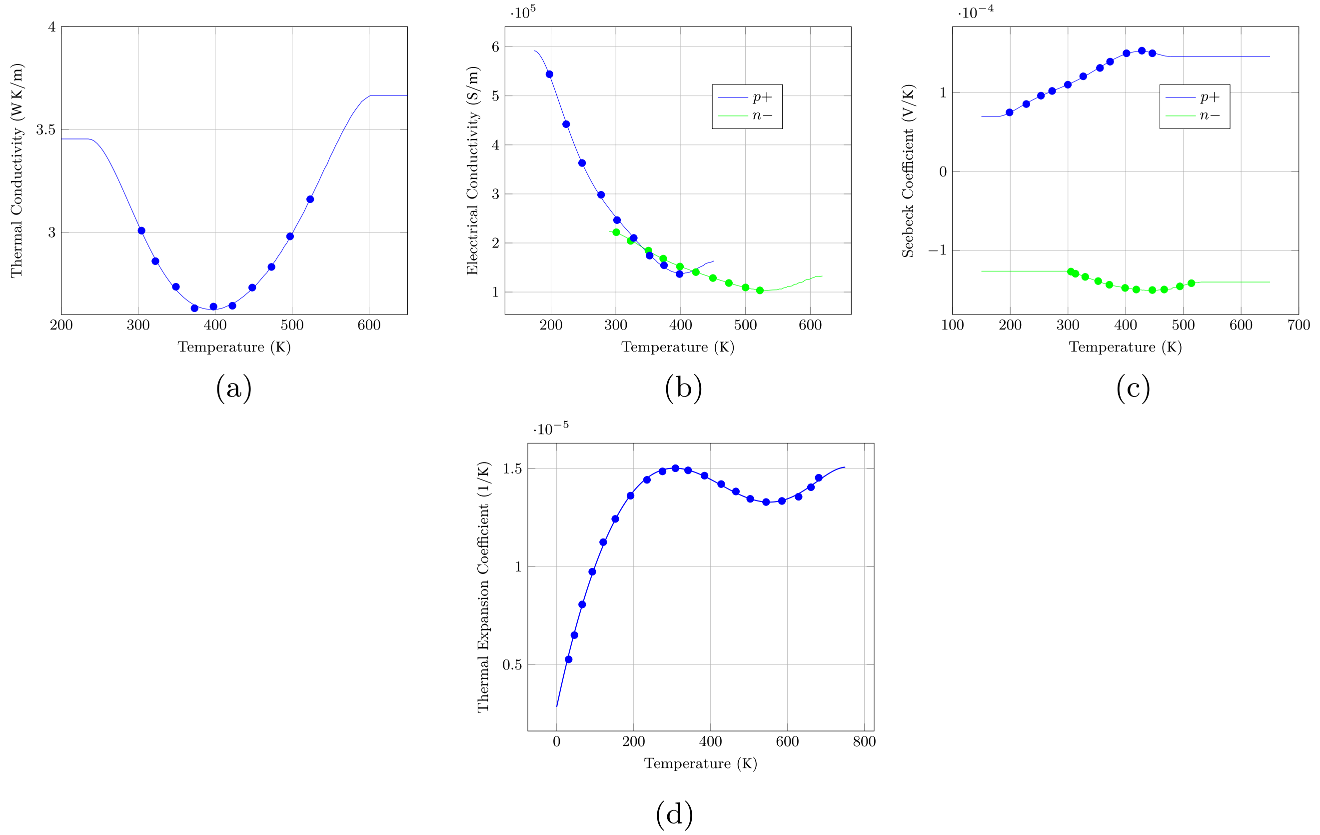

Fig. 11 Material properties of the semiconductor materials used in the optimization, including their Seebeck coefficients, and their thermal and electrical conductivities with respect to the temperature in °C. The results are plotted for the $p+$ and $n-$ semiconductors when the used data differ for each one of them

Table 7 Temperature constant material properties for the models used in Sect. 4

	E (GPa)	ν	κ (W K/m)	$\sigma \times 10^7$ (S/m)	$\alpha_T \times 10^{-6}$ (1/K)
Cu	130	0.34	385	59.9	17
AlN	300	0.21	319	–	5
SAC	70	0.42	50	8.5	24
Bi_2Te_3	61.6	0.241	Fig. 11	Fig. 11	Fig. 11
Air	–	–	0.033	–	–

Acknowledgements The authors thank the MTD collaboration members for their invaluable contributions.

Author contributions GRG http://orcid.org/0009-0000-0059-0918 wrote the main manuscript, developed the code, related simulations, and prepared all figures. All authors reviewed the manuscript.

Funding This material is based on work supported by the U.S. Department of Energy, Office of Science, and Office of High Energy Physics.

Data availability Data underlying the results presented in this paper are not publicly available at this time but may be obtained from the authors upon reasonable request.

Declarations

Conflict of interest The authors declare that they have no financial, personal, or other Conflict of interest that may have influenced the results or interpretations presented in this work.

Replication of results The code used to generate the results of this paper can be provided upon request. The results presented in Figs. 2 and 7 can be obtained through the implementation of the algorithm presented in Eq. (25) with the problem description provided in Sect. 4.

References

Ait Ouchaoui A, Nassraoui M, Radi B (2023) Numerical investigation of the effect of topology optimisation methods parameters in the topology quality, the strength, and the computational cost. Arch Mater Sci Eng 123(2):55–71. https://doi.org/10.5604/01.3001.0054.2492

Al-Fartoos MMR, Roy A, Mallick TK, Tahir AA (2023) Advancing thermoelectric materials: a comprehensive review exploring the significance of one-dimensional nano structuring. Nanomaterials. https://doi.org/10.3390/nano13132011

Al-Merbati AS, Yilbas BS, Sahin AZ (2013) Thermodynamics and thermal stress analysis of thermoelectric power generator: influence of pin geometry on device performance. Appl Therm Eng 50(1):683–692. https://doi.org/10.1016/j.applthermaleng.2012.07.021

Awrejcewicz J, Pavlov SP, Krysko AV, Zhigalov MV, Bodyagina KS, Krysko VA (2020) Decreasing shear stresses of the solder joints for mechanical and thermal loads by topological optimization. Materials. https://doi.org/10.3390/MA13081862

Bendsøe MP, Kikuchi N (1988) Generating optimal topologies in structural design using a homogenization method. Comput Methods Appl Mech Eng 71(2):197–224. https://doi.org/10.1016/0045-7825(88)90086-2

Bjørk R, Christensen D, Eriksen D, Pryds N (2014) Analysis of the internal heat losses in a thermoelectric generator. Int J Therm Sci 85:12–20. https://doi.org/10.1016/j.ijthermalsci.2014.06.003

Cai L, Li P, Luo Q, Yan H, Zhai P, Gao P (2020) Investigation of thermal radiation effects on thermoelectric module performance by an improved model. J Power Sour 477:228713. https://doi.org/10.1016/j.jpowsour.2020.228713

Chen WH, Wang CM, Lee DS, Kwon EE, Ashokkumar V, Culaba AB (2022) Optimization design by evolutionary computation for minimizing thermal stress of a thermoelectric generator with varied numbers of square pin fins. Appl Energy 314:118995. https://doi.org/10.1016/j.apenergy.2022.118995

Chen WY, Shi XL, Zou J, Chen ZG (2022) Thermoelectric coolers for on-chip thermal management: materials, design, and optimization. Mater Sci Eng R Rep 151(July):100700. https://doi.org/10.1016/j.mser.2022.100700

Duan M, Sun H, Lin B, Wu Y (2021) Evaluation on the applicability of thermoelectric air cooling systems for buildings with thermoelectric material optimization. Energy 221:119723. https://doi.org/10.1016/j.energy.2020.119723

Erturun U, Erermis K, Mossi K (2015) Influence of leg sizing and spacing on power generation and thermal stresses of thermoelectric devices. Appl Energy 159:19–27. https://doi.org/10.1016/j.apenergy.2015.08.112

Espadoto M, Rodrigues FC, Hirata NS, Telea AC (2023) Visualizing high-dimensional functions with dense maps. SN Comput Sci 4(3):1–18. https://doi.org/10.1007/s42979-022-01664-2

Fabián-Mijangos A, Min G, Alvarez-Quintana J (2017) Enhanced performance thermoelectric module having asymmetrical legs. Energy Conv Manage 148:1372–1381. https://doi.org/10.1016/j.enconman.2017.06.087

Fan S, Rezania A, Gao Y (2022) Thermal-electric and stress analysis of thermoelectric coolers under continuous pulse input current. Appl Therm Eng 214(June):118910. https://doi.org/10.1016/j.applthermaleng.2022.118910

Farrell PE, Birkisson FSW (2015) Deflation techniques for finding distinct solutions of nonlinear partial differential equations. SIAM J Sci Comput 37(4):A2026–A2045. https://doi.org/10.1137/140984798. arXiv: 1410.5620

Fernández E, Collet M, Alarcón P, Bauduin S, Duysinx P (2019) An aggregation strategy of maximum size constraints in density-based topology optimization. Struct Multidiscip Optim 60(5):2113–2130. https://doi.org/10.1007/s00158-019-02313-8

Fragoso OA, Orosco FAS, González JA, Georgiy L (2005) Linear theory of the thermoelectric cooling based on the peltier effect. 2nd international conference on electrical and electronics engineering, ICEEE and XI conference on electrical engineering, CIE 2005 2005(Cie):235–238, https://doi.org/10.1109/ICEEE.2005.1529616

Furuta K, Izui K, Yaji K, Yamada T, Nishiwaki S (2017) Level set-based topology optimization for the design of a peltier effect thermoelectric actuator. Struct Multidiscip Optim 55(5):1671–1683. https://doi.org/10.1007/s00158-016-1609-9

Gong T, Wu Y, Gao L, Zhang L, Li J, Ming T (2019) Thermo-mechanical analysis on a compact thermoelectric cooler. Energy 172:1211–1224. https://doi.org/10.1016/j.energy.2019.02.014

Goswami A, Kanetkar S (2020) Thermoelectrics in cryogenic cooling. 2020 IEEE 22nd electronics packaging technology conference. EPTC 2020:355–358. https://doi.org/10.1109/EPTC50525.2020.9315047

Gupta P, Tanwar A, He X, Gradkowski K, Razeeb KM, Morrissey PE, Brien PO (2024) Substrate integrated micro-thermoelectric coolers in glass substrate for next-generation photonic packages. J Opt Microsyst 4(1):1–18. https://doi.org/10.1117/1.JOM.4.1.011006

Gutiérrez GR, Fv K, Goosen JFL, Aragón AM, Bornheim A (2024) Enhancing the cooling performance of thermocouples: a power-constrained topology optimization procedure. Struct Multidiscip Optim 67(11):189. https://doi.org/10.1007/s00158-024-03897-6

Ibhadode O, Zhang Z, Rahnama P, Bonakdar A, Toyserkani E (2020) Topology optimization of structures under design-dependent pressure loads by a boundary identification-load evolution (bile) model. Struct Multidiscip Optim 62:1865–1883. https://doi.org/10.1007/s00158-020-02582-8

Lazarov B, Sigmund O (2011) Filters in topology optimization based on helmholtz-type differential equations. Int J Numer Meth Eng 86(6):765–781. https://doi.org/10.1002/nme.3072

Lazarov BS, Wang F, Sigmund O (2016) Length scale and manufacturability in density-based topology optimization. Arch Appl Mech 86(1):189–218. https://doi.org/10.1007/s00419-015-1106-4

Leblanc S, Yee SK, Scullin ML, Dames C, Goodson KE (2014) Material and manufacturing cost considerations for thermoelectrics.

Renew Sustain Energy Rev 32:313–327. https://doi.org/10.1016/j.rser.2013.12.030

Liu H, Li G, Zhao X, Ma X, Shen C (2023) Investigation of the impact of the thermoelectric geometry on the cooling performance and thermal‒mechanic characteristics in a thermoelectric cooler. Energy 267(2022):126471. https://doi.org/10.1016/j.energy.2022.126471

Lu T, Li Y, Zhang J, Ning P, Niu P (2020) Cooling and mechanical performance analysis of a trapezoidal thermoelectric cooler with variable cross-section. Energies. https://doi.org/10.3390/en13226070

Lundgaard C, Sigmund O (2018) A density-based topology optimization methodology for thermoelectric energy conversion problems. Struct Multidiscip Optim 57(4):1427–1442. https://doi.org/10.1007/s00158-018-1919-1

Maduabuchi C (2022) Thermo-mechanical optimization of thermoelectric generators using deep learning artificial intelligence algorithms fed with verified finite element simulation data. Appl Energy 315:118943. https://doi.org/10.1016/j.apenergy.2022.118943

Mativo J, Hallinan K, George U, Reich G, Steininger R (2020) Topology optimized thermoelectric generator: a parametric study. Energy Harv Syst 7(2):33–53. https://doi.org/10.1515/ehs-2021-0002

Meng Q, Xu B, Wang C, Zhao L (2021) Thermo-elastic topology optimization with stress and temperature constraints. Int J Numer Meth Eng 122(12):2919–2944. https://doi.org/10.1002/nme.6646

Merienne R, Lynn J, McSweeney E, O'Shaughnessy SM (2019) Thermal cycling of thermoelectric generators: the effect of heating rate. Appl Energy 237:671–681. https://doi.org/10.1016/j.apenergy.2019.01.041

Onodera S, Yamada T (2025) Topology optimization for coupled thermomechanical problems with approximated thermal radiation boundary conditions depending on design variables. Appl Math Model 142:115959. https://doi.org/10.1016/j.apm.2025.115959

Pavlova LM, Shtern YI, Mironov RE (2011) Thermal expansion of bismuth telluride. High Temp 49(3):369–379. https://doi.org/10.1134/S0018151X1103014X

Pérez-Aparicio JL, Taylor RL, Gavela D (2007) Finite element analysis of nonlinear fully coupled thermoelectric materials. Comput Mech 40(1):35–45. https://doi.org/10.1007/s00466-006-0080-7

Pérez-Aparicio JL, Palma R, Taylor RL (2016) Multiphysics and thermodynamic formulations for equilibrium and non-equilibrium interactions: non-linear finite elements applied to multi-coupled active materials. Arch Comput Methods Eng 23(3):535–583. https://doi.org/10.1007/s11831-015-9149-9

Pérez-Aparicio J, Moreno-Navarro P, Gómez-Hernández J (2024) Weighted sum optimization for combined thermoelectric geometry and electric pulse using finite elements. Appl Therm Eng 236:121599. https://doi.org/10.1016/j.applthermaleng.2023.121599

Rozvany GIN, Zhou M, Birker T (1992) Generalized shape optimization without homogenization. Struct Optim 4(3):250–252. https://doi.org/10.1007/BF01742754

Sharma R (2016) A stress recovery procedure for 3-D linear finite elements pp 1–86, https://resolver.tudelft.nl/uuid:97557770-5fc6-4930-b0d5-7476e2d0e050

Singh VK, Sisodia SS, Patel A, Shah T, Das P, Patel RN, Bhavsar RR (2023) Thermoelectric cooler (TEC) based thermal control system for space applications: numerical study. Appl Therm Eng 224(2022):120101. https://doi.org/10.1016/j.applthermaleng.2023.120101

Soprani S, Haertel JH, Lazarov BS, Sigmund O, Engelbrecht K (2016) A design approach for integrating thermoelectric devices using topology optimization. Appl Energy 176:49–64. https://doi.org/10.1016/j.apenergy.2016.05.024

Suhir E, Shakouri A (2013) Predicted thermal stress in a multileg thermoelectric module (TEM) design. J Appl Mech Trans ASME. https://doi.org/10.1115/1.4007524

Sun W, Wen P, Zhu S, Zhai P (2024) Geometrical optimization of segmented thermoelectric generators (tegs) based on neural network and multi-objective genetic algorithm. Energies. https://doi.org/10.3390/en17092094

Svanberg K (1987) The method of moving asymptotes‒a new method for structural optimization. Int J Numer Meth Eng 24(2):359–373. https://doi.org/10.1002/nme.1620240207

Svanberg K (2014) Mma and gcmma ‒ two methods for nonlinear optimization. https://api.semanticscholar.org/CorpusID:211105912

Takezawa A, Kitamura M (2012) Geometrical design of thermoelectric generators based on topology optimization. Int J Numer Meth Eng 90(11):1363–1392. https://doi.org/10.1002/nme.3375

Verbart A (2015) Topology optimization with stress constraints. PhD thesis, https://doi.org/10.13140/RG.2.1.3422.0880, https://repository.tudelft.nl/record/uuid:ee24b186-5db6-4c57-aa50-3b736110ff2a

Verbart A, Langelaar M, van Keulen F (2017) A unified aggregation and relaxation approach for stress-constrained topology optimization. Struct Multidiscip Optim 55(2):663–679. https://doi.org/10.1007/s00158-016-1524-0

Wang P, Li JE, Wang BL, Shimada T, Hirakata H, Zhang C (2019) Lifetime prediction of thermoelectric devices under thermal cycling. J Power Sour. https://doi.org/10.1016/j.jpowsour.2019.226861

Williams NP, Power J, Trimble D, O'Shaughnessy SM (2022) An experimental evaluation of thermoelectric generator performance under cyclic heating regimes. Heat Mass Trans Waerme Stoffuebertragung. https://doi.org/10.1007/s00231-022-03280-5

Witting IT, Chasapis TC, Ricci F, Peters M, Heinz NA, Hautier G, Snyder GJ (2019) The thermoelectric properties of Bismuth Telluride. Adv Electr Mater 5(6):1–20. https://doi.org/10.1002/aelm.201800904

Xing J, Wu M, Chen X, Zhan J (2024) Topology optimization design for voltage enhancement in variable structure double-layer flexible thermoelectric devices. Appl Math Model 136:115646. https://doi.org/10.1016/j.apm.2024.115646

Xu X, Wu Y, Zuo L, Chen S (2019) Multimaterial topology optimization of thermoelectric generators. Proceedings of the ASME design engineering technical conference 2A-2019(September 2021), https://doi.org/10.1115/DETC2019-97934

Yang RJ, Chen CJ (1996) Stress-based topology optimization. Struct Optim 12(2–3):98–105. https://doi.org/10.1007/BF01196941

Yvonnet J, Da D (2024) Topology optimization to fracture resistance: a review and recent developments. Arch Comput Methods Eng. https://doi.org/10.1007/s11831-023-10044-9

Zaferani SH, Sams MW, Ghomashchi R, Chen ZG (2021) Thermoelectric coolers as thermal management systems for medical applications: design, optimization, and advancement. Nano Energy 90:106572. https://doi.org/10.1016/j.nanoen.2021.106572

Zhang J, Zhao H, Feng B, Song X, Zhang X, Zhang R (2023) Numerical simulations and optimized design on the performance and thermal stress of a thermoelectric cooler. Int J Refrig 146:314–326. https://doi.org/10.1016/j.ijrefrig.2022.11.010

Zhang W, Shen L, Yang Y, Chen H (2015) Thermal management for a micro semiconductor laser based on thermoelectric cooling. Appl Therm Eng 90:664–673. https://doi.org/10.1016/j.applthermaleng.2015.07.027

Zhou M, Lazarov BS, Wang F, Sigmund O (2015) Minimum length scale in topology optimization by geometric constraints. Comput Methods Appl Mech Eng 293:266–282. https://doi.org/10.1016/j.cma.2015.05.003